RIM-BP2 regulates Ca^{2+} channel abundance and neurotransmitter release at hippocampal mossy fiber terminals.

Rinako Miyano[1], Hirokazu Sakamoto[2], Kenzo Hirose[2, 3], and Takeshi Sakaba[1]

[1]Graduate School of Brain Science, Doshisha University, Kyotanabe-shi, Kyoto 610-0394, Japan

[2]Department of Pharmacology, Graduate School of Medicine, The University of Tokyo, Bunkyo-ku, Tokyo 113-0033, Japan

[3]International Research Center for Neurointelligence (WPI-IRCN), The University of Tokyo, Bunkyo-ku, Tokyo 113-0033, Japan

Abstract

Synaptic vesicles dock and fuse at the presynaptic active zone (AZ), the specialized site for transmitter release. AZ proteins play multiple roles such as recruitment of Ca^{2+} channels as well as synaptic vesicle docking, priming and fusion. However, the precise role of each AZ protein type remains unknown. In order to dissect the role of RIM-BP2 at mammalian cortical synapses having low release probability, we applied direct electrophysiological recording and super-resolution imaging to hippocampal mossy fiber

terminals of RIM-BP2 KO mice. By using direct presynaptic recording, we found the reduced Ca^{2+} currents. The measurements of EPSCs and presynaptic capacitance suggested that the initial release probability was lowered because of the reduced Ca^{2+} influx and impaired fusion competence in RIM-BP2 KO. Nevertheless, larger Ca^{2+} influx restored release partially. Consistent with presynaptic recording, STED microscopy suggested less abundance of P/Q-type Ca^{2+} channels at AZs deficient in RIM-BP2. Our results suggest that the RIM-BP2 regulates both Ca^{2+} channel abundance and transmitter release at mossy fiber synapses.

Introduction

At chemical synapses, an action potential arriving at the presynaptic terminal opens voltage-gated Ca^{2+} channels, and Ca^{2+} influx through voltage-gated Ca^{2+} channels triggers neurotransmitter release from synaptic vesicles within milliseconds. Synaptic vesicle fusion occurs at a specialized region of the presynaptic membrane called the active zone (AZ), where Ca^{2+} channel clusters and vesicle fusion sites are accommodated via AZ scaffold proteins (Südhof, 2012). For rapid transmission, accumulation of Ca^{2+} channels, co-localization of Ca^{2+} channels and fusion sites, and molecular priming of synaptic vesicles for fusion are required, and the differences among these factors might provide a basis for synaptic diversity. However, it remains unknown how these factors are regulated by AZ-

37 scaffold proteins.

38 Rab3-interacting molecule-binding proteins (RIM-BPs) represent one principal,
39 conserved family of AZ proteins and bind to RIMs and Ca^{2+} channels (Wang et al., 2000;
40 Hibino et al., 2002). RIM-BP family includes RIM-BP1, RIM-BP2, and RIM-BP3 in mammals,
41 but RIM-BP3 expression is low in the nervous system (Mittelstaedt and Schoch, 2007). In
42 *Drosophila* neuromuscular junctions (NMJs), loss of RIM-BPs decreases Ca^{2+} channel
43 density and reduces release probability (Liu et al., 2011). Moreover, RIM-BP in *Drosophila*
44 NMJs is necessary for tight coupling of synaptic vesicles to Ca^{2+} channels and replenishment
45 of high release probability vesicles (Liu et al., 2011; Müller et al., 2015; Petzoldt et al., 2020).
46 In mammalian synapses, the observations from KO mice are diverse. In RIM-BP1,2 DKO
47 mice, the coupling between Ca^{2+} channels and synaptic vesicles becomes loose, and action
48 potential-evoked neurotransmitter release is reduced at the calyx of Held synapse (Acuna et
49 al., 2015; Butola et al., 2021). At hippocampal CA3-CA1 synapses, RIM-BP2 deletion alters
50 Ca^{2+} channel localization at the AZs without altering total Ca^{2+} influx. Besides, RIM-BP1,2
51 DKO has no additional effect, indicating that RIM-BP2 dominates the function of RIM-BP
52 isoforms (Grauel et al., 2016; see also Krinner et al., 2021). Tight coupling between Ca^{2+}
53 channels and vesicles is crucial for rapid and efficient transmitter release (Wadel et al., 2007).

54 In contrast, hippocampal mossy fiber-CA3 synapses are characterized by low

55 release probability (Vyleta and Jonas, 2014). At hippocampal mossy fiber synapses, gSTED
56 imaging suggests that RIM-BP2 KO alters the Munc13-1 cluster number and distribution. In
57 addition, RIM-BP2 deletion decreases the number of docked vesicles (Brockmann et al.,
58 2019). However, because of technical difficulty, direct and quantitative measurements of
59 exocytosis in RIM-BP2 KO terminals have not been performed so far.

60 To quantify the RIM-BP2 function in mossy fiber-CA3 synapses, we performed
61 whole-cell patch-clamp recordings from WT and RIM-BP2 KO hippocampal mossy fiber
62 boutons. From electrophysiological recordings, we found that the reductions of Ca^{2+} current
63 amplitudes in RIM-BP2 KO terminals. The EPSC and capacitance measurements suggested
64 that the reduction of Ca^{2+} currents was responsible, in part, for that of transmitter release. In
65 addition, they suggested that fusion competence was impaired, which could be overcome by
66 larger Ca^{2+} influx into the terminal. Using STED imaging, we found the abundance of P/Q-
67 type Ca^{2+} channels in terminals to be reduced in RIM-BP2 KO. We suggest that RIM-BP2
68 regulates the number of P/Q-type Ca^{2+} channels at the AZ and is critical for transmitter
69 release at hippocampal mossy fiber terminals.

70

71 **Results**

72 **RIM-BP2 KO reduces presynaptic calcium currents at hippocampal mossy fiber**

73 **boutons.**

74 To investigate the roles of RIM-BP2 in synaptic transmission, we examined the
75 kinetics of exocytosis and Ca^{2+} influx in WT and RIM-BP2 KO synapses using presynaptic
76 whole-cell capacitance measurements (Fig. 1). When the terminal was depolarized from -80
77 mV to +10 mV for 10 ms, Ca^{2+} currents and membrane capacitance were recorded as shown
78 in Fig. 1A. During the depolarizing pulse, capacitance was not measured due to large
79 conductance changes, and the increase was used for measuring synaptic vesicle exocytosis.
80 To determine the size of the RRP and the time course of exocytosis, we measured
81 capacitance changes (ΔC_m) in response to various durations of depolarization. Here, the
82 length of the depolarizing pulse was varied between 5 ms and 100 ms, and ΔC_m was plotted
83 against pulse duration (Fig. 1B and Figure 1-figure supplement 1, bottom). ΔC_m became
84 larger as the duration of pulse was prolonged, but the increase started to be saturated at a
85 100 ms pulse in WT terminals, suggesting depletion of the RRP. ΔC_m in response to a 100
86 ms pulse was 52 ± 8.1 fF (n = 9, Fig. 1B). The amplitude corresponds to the fusion of about
87 500-600 synaptic vesicles (Hallermann et al., 2003; Midorikawa and Sakaba, 2017). The time
88 course of ΔC_m could be fitted by a single exponential with a time constant of 59 ± 12 ms. In
89 RIM-BP2 KO terminals, ΔC_m in response to a 100 ms pulse was somewhat smaller (41 ± 5.9
90 fF, n = 8) than that of WT terminals, and the release time constant was somewhat slower (64

91 ± 14 ms) than in WT terminals. We should note that the time constant is not necessarily
92 reliable because the ΔC_m values do not reach a plateau value at 100 ms pulse in some
93 terminals. Although the capacitance jumps of KO may be smaller for shorter pulses,
94 capacitance measurements are not sensitive enough to detect small changes (< 5 fF, 50
95 vesicles, see Fig. 5 & Fig. 6). Nevertheless, the differences in the time course of capacitance
96 were not significantly different between WT and KO ($p = 0.23$ from ANOVA) and the effects
97 on release examined by strong pulses depleting the RRP was relatively minor. The
98 amplitudes of Ca^{2+} currents were smaller in RIM-BP2 KO terminals as compared to WT
99 terminals (Fig. 1B and Figure 1-figure supplement 1, top, $p < 0.02$ from ANOVA). The Ca^{2+}
100 current in response to a 100 ms pulse was reduced by ~30% in RIM-BP2 KO terminals (27
101 ± 3.9 pA, n = 8) compared to WT terminals (44 ± 5.4 pA, n = 9) ($p = 0.0248$, t-test, Fig. 1B).
102 Thus, the results show that RIM-BP2 deletion reduces presynaptic Ca^{2+} influx, but effects on
103 the RRP size and the time course of release measured by capacitance measurements are
104 relatively minor.

105 To investigate the Ca^{2+} influx in more detail, we examined the voltage dependence
106 of Ca^{2+} currents. Fig. 1C shows voltage step protocols and representative current traces. In
107 both genotypes, Ca^{2+} currents started to be activated at around -20 mV, and maximal
108 amplitude was observed at ~+10 mV (Fig. 1D). There was no major difference in the voltage

109 dependence of Ca^{2+} currents between WT and RIM-BP2 KO mice. Consistently, activation

110 time constants of Ca^{2+} currents were similar between WT and RIM-BP2 KO, when the

111 terminal was depolarized to +10 mV (τ = 1.4 ± 0.2 ms in WT, n = 6; τ = 1.3 ± 0.2 ms in KO, n

112 = 4). These results suggest a reduction in the number of Ca^{2+} channels rather than changes

113 in activation kinetics is responsible for the current decrease observed.

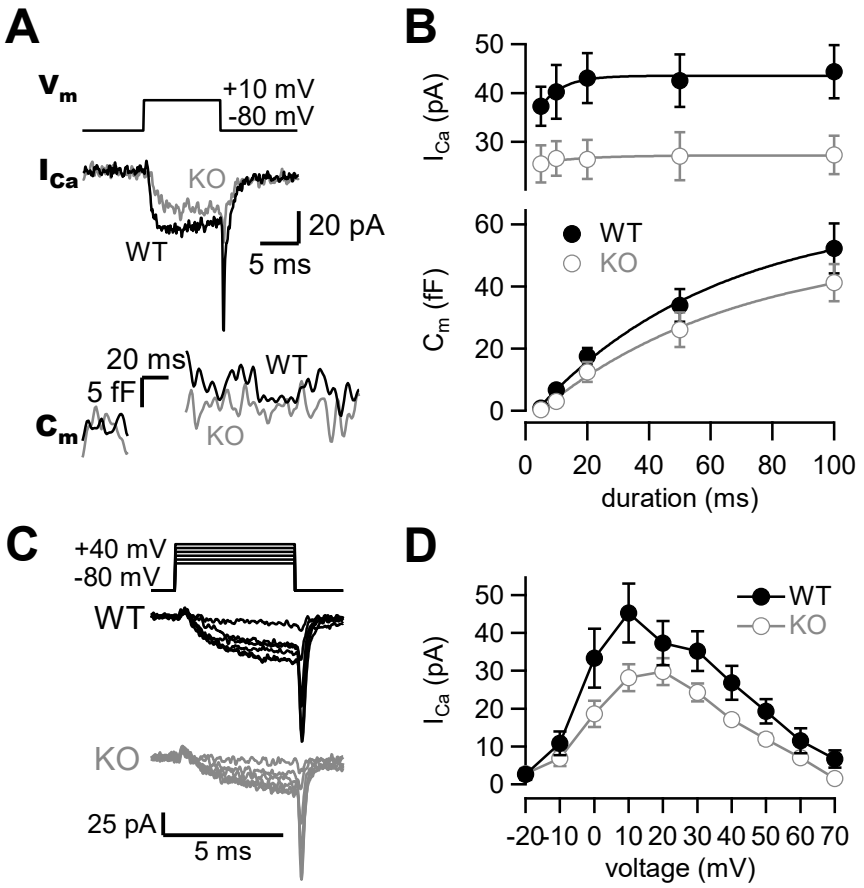

114

115 **Figure 1. Presynaptic calcium currents and synaptic vesicle release in RIM-BP2 KO**

116 **mice**

117 (**A**) The terminal was depolarized from -80 mV to +10 mV in WT (black) and RIM-BP2 KO

118 (gray) hippocampal mossy fiber boutons. Ca^{2+} currents (I_{Ca}) and membrane capacitance (C_m)

119 in response to a 10 ms pulse (V_m) are shown. (**B**) *(top)* The peak Ca^{2+} currents are plotted

120 against the pulse duration. WT vs KO, p = 0.034 (ANOVA). *(bottom)* The capacitance jumps

121 are plotted against the pulse duration. WT vs KO, p = 0.23 (ANOVA). Black filled circles and

122 gray open circles represent the data from WT (n = 9 from 8 animals) and RIM-BP2 KO (n =

123 8 from 6 animals), respectively. Each data point represents mean ± SEM. (**C**) Experimental

124 protocol and representative traces for presynaptic Ca^{2+} current measurements in WT (black)

125 and RIM-BP2 KO (gray) boutons. Terminals were sequentially depolarized for 5 ms with 2

126 ms intervals from -80 mV to +70 mV by 10 mV steps. (**D**) Current-voltage relationships of

127 peak Ca^{2+} currents in WT (black filled circle; n = 4-6 from 4 animals) and RIM-BP2 KO (gray

128 open circle; n = 4-5 from 5 animals). I_{Ca}s were elicited by 5 ms depolarizations. Two curves

129 were significantly different ($p < 0.01$ from mixed model). Each data point represents mean ±

130 SEM. Numerical values of plots are provided in Figure 1-source data 1.

131

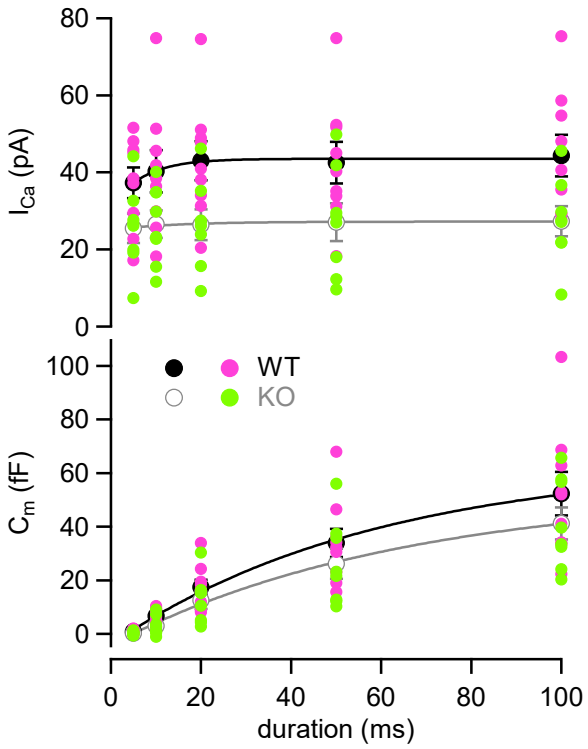

Figure 1-figure supplement 1. Individual value plot of Fig. 1B

Individual values of I_{Ca}s (*top*) and C_ms (*bottom*) in WT (pink) and RIM-BP2 KO (green) terminals are plotted against the pulse duration. Numerical values of plots are provided in Figure 1-source data 1.

Figure 1-source data 1. Datasets of Ca^{2+}-current and capacitance amplitudes presented in Figure 1 and Figure 1-figure supplement 1.

The effects of extracellular calcium concentration on Ca^{2+} influx and capacitance changes in WT and RIM-BP2 KO.

Because Ca^{2+} currents were reduced in RIM-BP2 KO mice, we tested whether the

143 reduction of Ca^{2+} currents could be restored by elevation of the external Ca^{2+} concentration.

144 We raised the extracellular Ca^{2+} concentration ($[Ca^{2+}]_{ext}$) from 2 mM to 4 mM (Fig. 2). Ca^{2+}

145 currents and membrane capacitances were recorded at 4 mM $[Ca^{2+}]_{ext}$, and amplitudes then

146 plotted against pulse duration (Fig. 2A and Figure 2-figure supplement 1). Although Ca^{2+}

147 current elicited by a 100 ms pulse in RIM-BP2 KO was still smaller (33 ± 2.7 pA, n = 3) than

148 that in WT (54 ± 6.1 pA, n = 6) (Fig. 2B, top) in 4 mM Ca^{2+}, Ca^{2+} currents of KO mice at 4

149 mM $[Ca^{2+}]_{ext}$ were more comparable to those of WT at 2 mM $[Ca^{2+}]_{ext}$.

150 At 4 mM $[Ca^{2+}]_{ext}$, ΔC_m in response to a 100 ms pulse in RIM-BP2 KO was 51 ± 11

151 fF (n = 3) and showed a similar value in WT at 2 mM $[Ca^{2+}]_{ext}$ (Fig. 2B, bottom). At the same

152 time, ΔC_m in WT was not altered (52 ± 2.5 fF, n = 6) at higher $[Ca^{2+}]_{ext}$. The time course of

153 exocytosis at 4 mM $[Ca^{2+}]_{ext}$ in KO was similar to that of WT at 2 mM $[Ca^{2+}]_{ext}$, as the time

154 courses were superimposable in Fig. 2A (p = 0.57 from mixed model).

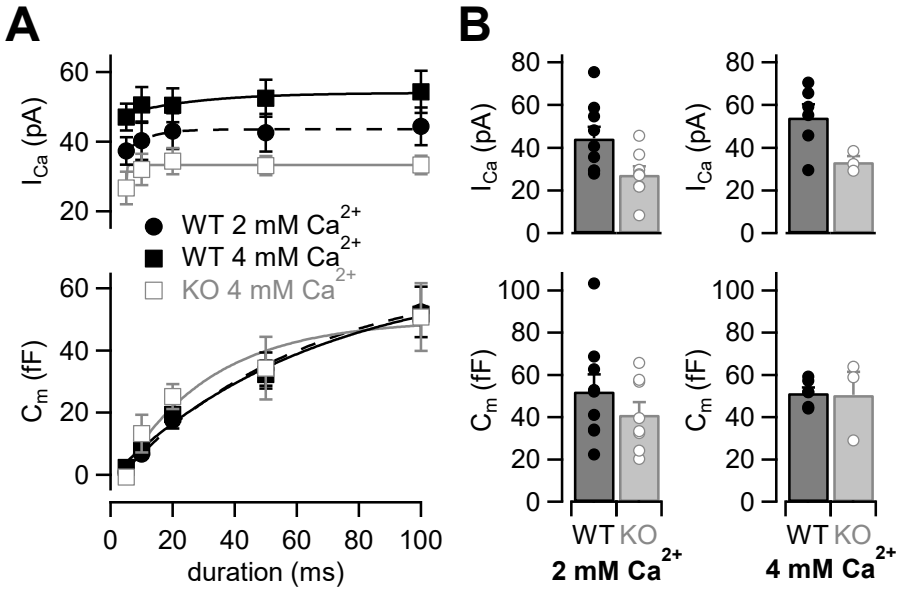

155

156 **Figure 2. The effects of high extracellular calcium concentration on Ca^{2+} currents and**

157 **capacitance changes.**

158 (**A**) The I_{Ca}s (*top*) and the C_ms (*bottom*) are plotted against the pulse duration. Black filled

159 squares and gray open squares represent the data from WT (n = 6-8 from 6 animals) and

160 RIM-BP2 KO (n = 3-4 from 2 animals) at 4 mM $[Ca^{2+}]_{ext}$, respectively. For comparison, the

161 WT data in 2 mM $[Ca^{2+}]_{ext}$ are superimposed (black filled circle; n = 9) (the same data sets

162 as Fig. 1B). Each data point represents mean ± SEM. I_{Ca}s were significantly different between

163 WT and KO in 4 mM $[Ca^{2+}]_{ext}$ ($p < 0.01$ from mixed model). The WT I_{Ca}s in 2 mM $[Ca^{2+}]_{ext}$ and

164 the KO I_{Ca}s in 4 mM $[Ca^{2+}]_{ext}$ were significantly different ($p < 0.02$ from mixed model), but Cm

165 were not significantly different ($p = 0.57$ from mixed model). (**B**) Average I_{Ca}s *(top)* and C_ms

166 *(bottom)* in response to a 100 ms pulse in WT (black bars) and RIM-BP2 KO (gray bars)

167 terminals. Extracellular Ca^{2+} concentration was 2 mM *(left)* or 4 mM *(right)*. Error bars show

168 SEM. Circles indicate individual values. Numerical values of plots are provided in Figure 2-

169 source data 1.

170

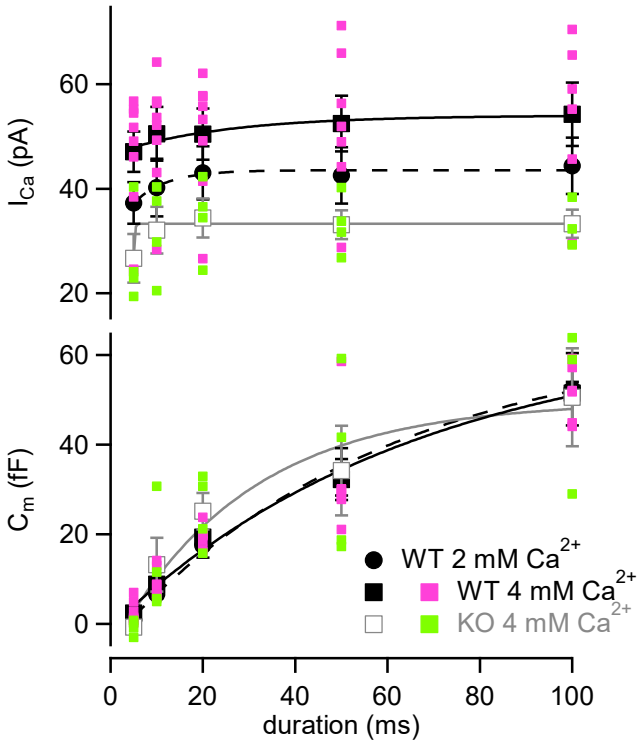

171

172 **Figure 2-figure supplement 1. Individual value plot of Fig. 2A**

173 Individual values of I_{Ca}s (*top*) and C_ms (*bottom*) recorded at 4 mM $[Ca^{2+}]_{ext}$ in WT (pink) and

174 RIM-BP2 KO (green) terminals are plotted against the pulse duration. Numerical values of

175 plots are provided in Figure 2-source data 1.

176 **Figure 2-source data 1.** Datasets of Ca^{2+}-current and capacitance amplitudes presented in

177 Figure 2 and Figure 2-figure supplement 1.

178

179 Next, we adjusted Ca^{2+} current amplitudes of WT to that of RIM-BP2 KO by lowering

180 $[Ca^{2+}]_{ext}$ (Fig. 3). The amplitudes of Ca^{2+} currents and capacitance jumps were plotted against

181 pulse duration (Fig. 3A and Figure 3-figure supplement 1). At 1 mM $[Ca^{2+}]_{ext}$, Ca^{2+} currents

182 and ΔC_m were smaller than those of RIM-BP2 KO at 2 mM $[Ca^{2+}]_{ext}$. At 1.5 mM $[Ca^{2+}]_{ext}$, Ca^{2+}

183 currents became more comparable to those of RIM-BP2 KO at 2 mM $[Ca^{2+}]_{ext}$ ($p = 0.12$ from

184 mixed model). Here, the ΔC_m evoked by a 100 ms pulse (43 ± 6.7 fF, n = 5) was comparable

185 between WT and RIM-BP2 KO (Fig. 3A). The average time course of capacitance increase

186 of WT at 1.5 mM $[Ca^{2+}]_{ext}$ was similar to that of RIM-BP2 KO at 2 mM $[Ca^{2+}]_{ext}$ ($p = 0.88$ from

187 mixed model). Therefore, by reducing Ca^{2+} currents, WT data could reproduce similar release

188 time course of RIM-BP2 KO. In Fig. 3B, ΔC_m in response to a 100 ms pulse at various

189 $[Ca^{2+}]_{ext}$s were plotted against the peak Ca^{2+} current amplitudes. The relationship could be

190 fitted by a Hill plot with n = 3 in WT (Schneggenburger et al., 1999). Consistently, when

191 capacitance jumps elicited by various pulse durations are plotted against total Ca^{2+} influx

192 (Figure 3-figure supplement 2), the RIM-BP2 KO data were superimposed on the WT data.

193 In Fig. 3C, relative amplitudes of Ca^{2+} currents and capacitance in response to a 100 ms

194 pulse are plotted. The RIM-BP2 KO data were superimposed on the WT data, suggesting

195 that the RRP size were similar between WT and KO (~50 fF). Taken together, presynaptic

196 capacitance measurements were not able to detect differences in the release rates between

197 WT and KO especially when Ca^{2+} influx in WT and KO was adjusted to be similar. In particular,

198 the RRP sizes measured by the pool depleting stimulation were not altered strongly by RIM-

199 BP2 KO. The results may mean that RIM-BP2 is dispensable for transmitter release or that

200 large Ca^{2+}, or large Ca^{2+} influx may overcome the deficit of the release. Alternatively,

201 capacitance measurements may not be sensitive enough to detect the differences between

202 WT and KO at short stimulation, which are relevant for AP-evoked release (see below, Fig. 5

203 and Fig. 6).

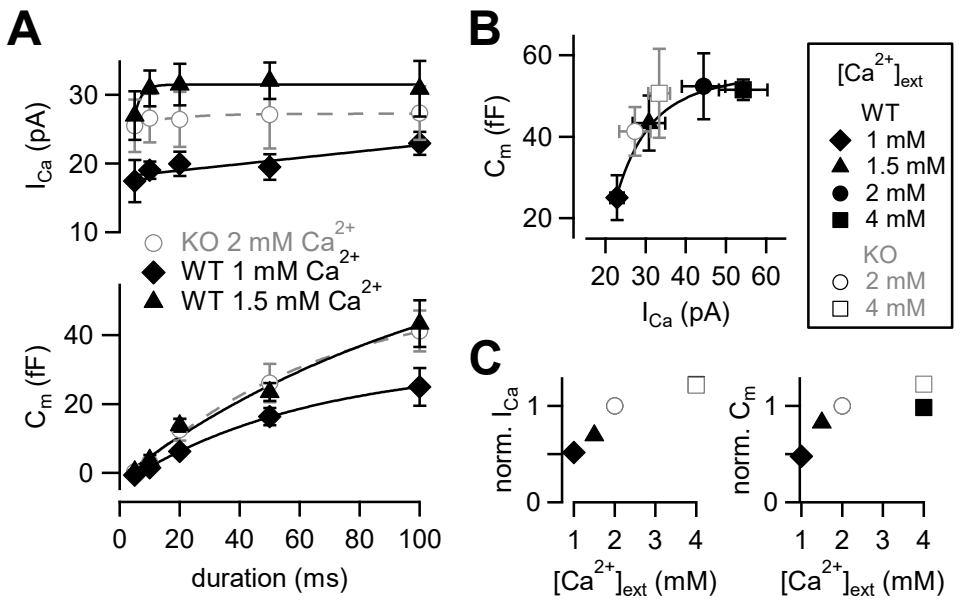

204

205 **Figure 3. Calcium-dependence of the release kinetics and the RRP size**

206 (**A**) *(top)* The relationship between peak Ca^{2+} currents and pulse durations at different

207 $[Ca^{2+}]_{ext}$s. *(bottom)* The relationship between capacitance jumps and pulse durations at

208 different $[Ca^{2+}]_{ext}$s. Gray open circles, black diamonds and black triangles represent the data

209 from RIM-BP2 KO at 2 mM $[Ca^{2+}]_{ext}$ (n = 8) (the same data sets as Fig. 1B), WT at 1 mM

210 $[Ca^{2+}]_{ext}$ (n = 3-5 from 4 animals) and WT at 1.5 mM $[Ca^{2+}]_{ext}$ (n = 5-7 from 6 animals),

211 respectively. Each data point represents mean ± SEM. (**B**) Capacitance jumps at various

212 $[Ca^{2+}]_{ext}$s are plotted against calcium current amplitudes. Pulses were 100 ms depolarization

213 from -80 mV to +10 mV. Each data point represents mean ± SEM. Data points were fitted

214 with a Hill equation with n = 3. (**C**) *(left)* Average I_{Ca}s at indicated $[Ca^{2+}]_{ext}$s were normalized

215 to the response at 2 mM $[Ca^{2+}]_{ext}$ in each genotype. *(right)* Average C_ms at indicated $[Ca^{2+}]_{ext}$s

216 were normalized to the 2 mM $[Ca^{2+}]_{ext}$ response in each genotype. Numerical values of plots

217 are provided in Figure 3-source data 1.

218

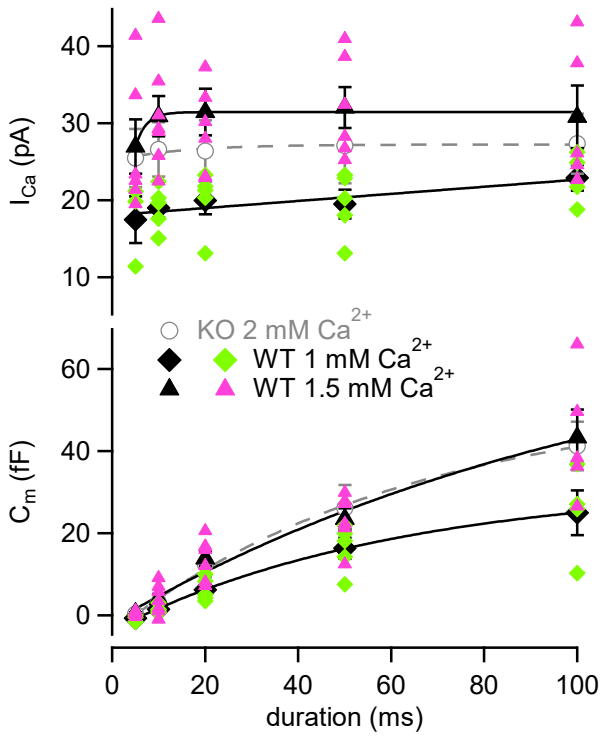

219

220 **Figure 3-figure supplement 1. Individual value plot of Fig. 3A**

221 Individual values of I_{Ca}s (*top*) and C_ms (*bottom*) recorded at 1 mM (green) or 1.5 mM (pink)

222 $[Ca^{2+}]_{ext}$ in WT are plotted against the pulse duration. Numerical values of plots are provided

223 in Figure 3-source data 1.

224 **Figure 3-source data 1.** Datasets of numerical values presented in Figure 3 and Figure 3-

225 figure supplement 1,

226

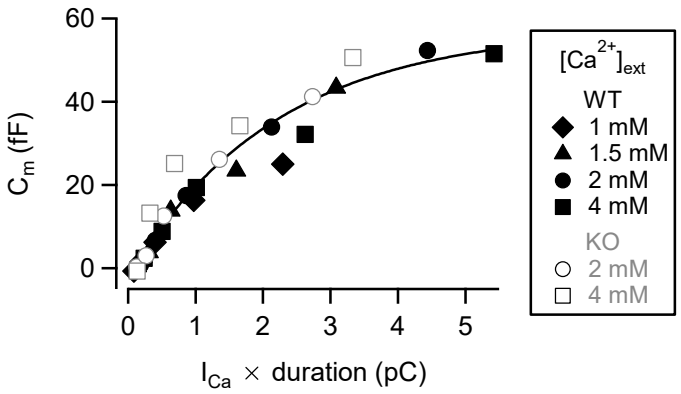

227

228 **Figure 3-figure supplement 2. The relationship between synaptic vesicle release and**

229 **total Ca^{2+} charge**

230 Capacitance jumps elicited by various pulse durations are plotted against total Ca^{2+} charge.

231 The total Ca^{2+} charge was calculated by multiplying a peak Ca^{2+} current amplitude by pulse

232 duration. Each symbol represents a data point obtained from WT (black filled symbols) and

233 RIM-BP2 KO (gray open symbols) mice at various $[Ca^{2+}]_{ext}$. Data points were fitted by a single

234 exponential function. Numerical values of plots are provided in Figure 3-figure supplement

235 2-source data 1.

236 **Figure 3-figure supplement 2-source data 1.** Datasets of Ca^{2+} charge and ΔC_m presented

237 in Figure 3-figure supplement 2.

238

239 **High EGTA experiments suggest unaltered coupling between calcium channels and**

240 **synaptic vesicles.**

241 Previous studies have used Ca^{2+} chelator such as EGTA to examine the sensitivity

242 of release to intracellular Ca^{2+} buffers (Adler et al., 1991; Borst & Sakmann, 1996; Vyleta &

243 Jonas, 2014). When the physical coupling between Ca^{2+} channels and synaptic vesicles is

244 tight, EGTA (slow Ca^{2+} chelator) has less effect on release probability, but EGTA is effective

245 when the coupling is loose. Previous experiments have suggested that RIM-BPs regulated

246 the channel-vesicle coupling at the calyx of Held (Acuna et al., 2015). If this observation also

247 applies to the mossy fiber synapse, EGTA sensitivity of release should be higher in RIM-BP2

248 KO terminals. To investigate the coupling at mossy fiber boutons in RIM-BP2 KO, we

249 changed the concentration of EGTA in the patch pipette. In the presence of 5 mM EGTA, we

250 depolarized the terminal from -80 mV to +10 mV for 5 ms and recorded Ca^{2+} currents and

251 membrane capacitance (Fig. 4A). Ca^{2+} currents and ΔC_m were plotted against pulse duration

252 (Fig. 4B and Figure 4-figure supplement 1). In both WT and RIM-BP2 KO mice, ΔC_m were

253 reduced under 5 mM EGTA compared with the control condition of 0.5 mM EGTA. We

254 compared the effect of EGTA on average amplitudes of peak Ca^{2+} currents in response to a
255 20 ms pulse (Fig. 4D). Interestingly, Ca^{2+} current amplitudes were ~1.2 times larger at 5 mM
256 EGTA (53 ± 12 pA, n = 5) than at 0.5 mM EGTA (43 ± 5.1 pA, n = 9) in WT, though the data
257 scattered under 5 mM EGTA condition and there was no statistically significant difference (p
258 = 0.36, t-test). In RIM-BP2 KO, we did not observe such an increase. EGTA might inhibit Ca^{2+}
259 channel inactivation in WT (von Gersdorff and Matthews, 1996). In Fig. 4C, we compared the
260 effect of EGTA on the ΔC_m in response to a 20 ms pulse. In both genotypes, ΔC_m values
261 were inhibited by 5 mM EGTA, and the inhibition was somewhat larger in RIM-BP2 KO (EGTA
262 inhibition: $p < 0.01$, genotypes $p > 0.05$ from mixed model).

263 Ca^{2+} current amplitudes in RIM-B2 KO are smaller than in WT (Fig. 4B). It is possible
264 that strong effect of high EGTA on release may be due to reduced Ca^{2+} currents in RIM-BP2
265 KO. Therefore, we changed $[Ca^{2+}]_{ext}$ from 2 mM to 1 mM and adjusted Ca^{2+} current
266 amplitudes of WT to the RIM-BP2 KO level. The capacitance increase and the amplitudes of
267 Ca^{2+} currents became similar to those of RIM-BP2 KO (Fig. 4C and Fig. 4D). These results
268 indicated that WT and RIM-BP2 KO terminals had similar sensitivity of neurotransmitter
269 release to EGTA. Thus, it is unlikely that changes in the coupling distance are responsible
270 for the reduced exocytosis of the mutants.

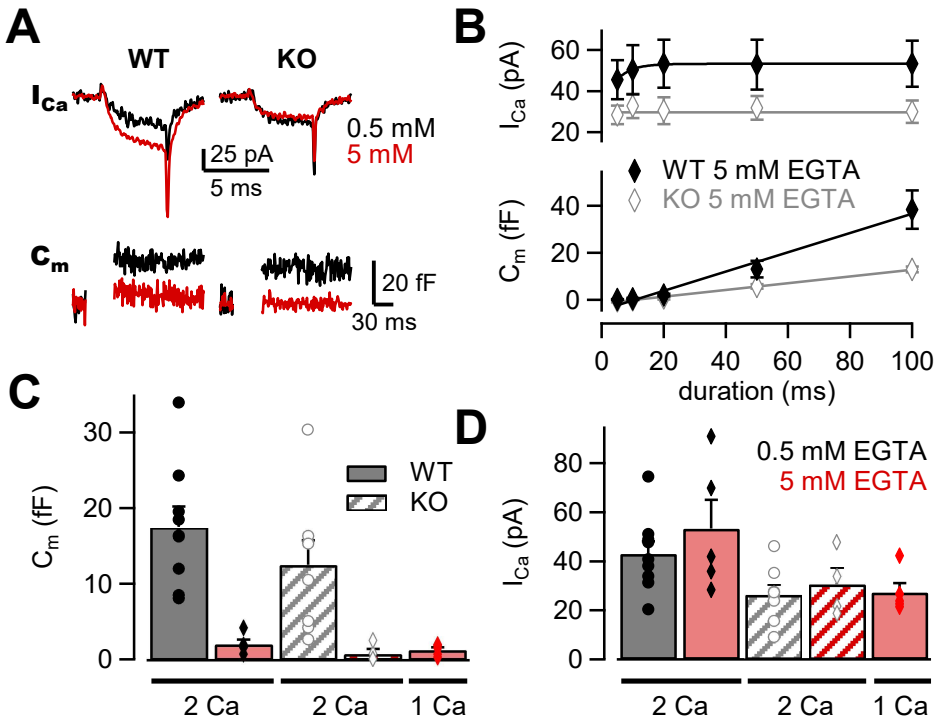

Figure 4. The effects of high EGTA on calcium currents and synaptic vesicle exocytosis

(**A**) Example traces in response to a 5 ms depolarizing pulse to +10 mV in WT *(left)* and RIM-BP2 KO *(right)* boutons. Ca^{2+} current (I_{Ca}) and membrane capacitance (C_m) recorded with 0.5 mM EGTA (black) or 5 mM EGTA (red) in the patch pipette are shown. Note that each trace was obtained from different terminals but the traces were superimposed. (**B**) The I_{Ca}s *(top)* and C_ms *(bottom)* are plotted against the pulse duration. The patch pipette contained 5 mM EGTA. Black filled diamonds and gray open diamonds represent the data from WT (n = 4-5 from 4 animals) and RIM-BP2 KO (n = 4 from 3 animals), respectively. Each data point indicates mean ± SEM. (**C, D**) Average C_ms (**C**) and I_{Ca}s (**D**) elicited by a 20 ms pulse in WT

282 (filled bars) and RIM-BP2 KO (hatched bars). The extracellular Ca^{2+} concentration was 1 mM

283 (from 5 animals) or 2 mM. The intracellular solution contained either 0.5 mM EGTA (black) or

284 5 mM EGTA (red). Error bars show SEM. Circles and diamonds indicate individual values.

285 Numerical values of plots are provided in Figure 4-source data 1.

286

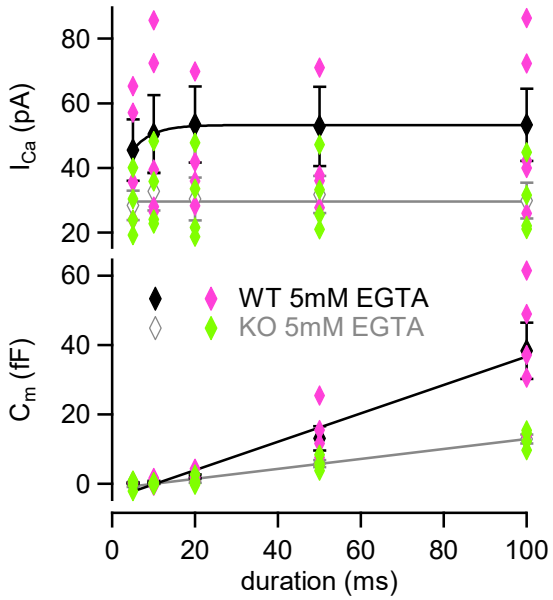

287

288 **Figure 4-figure supplement 1. Individual value plot of Fig. 4B**

289 Individual values of I_{Ca}s (*top*) and C_ms (*bottom*) recorded in the presence of 5 mM EGTA in

290 WT (green) and KO (pink) were plotted against the pulse duration. Numerical values of plots

291 are provided in Figure 4-source data 1.

292 **Figure 4-source data 1.** Datasets of Ca^{2+}-current and capacitance amplitudes presented in

293 Figure 4 and Figure 4-figure supplement 1.

294

295 **Smaller AP-evoked EPSCs in KO could not be explained entirely by the reduced Ca^{2+}**

296 **influx.**

297 While Ca^{2+} current amplitudes were clearly reduced in KO, capacitance jumps were

298 reduced little. Capacitance measurements could only detect large amounts of exocytosis (~5

299 fF, 50 vesicles), and the changes relevant for the AP-evoked release (< 10 vesicles per AP

300 per synapse) could not be detected. Moreover, large Ca^{2+} influx used for the stimulation

301 protocol of Fig.1 to Fig. 3 could overcome the deficits of RIM-BP2 KO. In order to detect the

302 changes related to physiological conditions, we measured the AMPA-EPSCs evoked by

303 electrical mossy fiber stimulation at CA3 pyramidal cells (Fig. 5). As seen in Fig. 5A and Fig.

304 5B, the EPSCs were evoked by dual stimulation of mossy fibers. The mossy-fiber evoked

305 responses were confirmed by the relatively faster EPSC kinetics and sensitivity to DCG-Ⅳ

306 (1 μM), a mGluR2 agonist (remaining response of < 30 %, 0.23 ± 0.01 for WT (n = 5), 0.29 ±

307 0.02 for KO (n = 5)). Because multiple fibers were stimulated, we could not estimate the

308 number of vesicles released per one synapse. Nevertheless, when fibers were stimulated

309 similarly, the EPSC amplitudes of KO were much smaller (893 ± 202 pA in WT, n = 7; 189 ±

310 73 pA in KO, n = 7) (p = 0.011). In Fig. 2, Presynaptic recordings indicated that Ca^{2+} current

311 amplitudes of KO at 4 mM $[Ca^{2+}]_{ext}$ became similar to those of WT at 2 mM $[Ca^{2+}]_{ext}$ (Fig. 2).

312 The EPSCs became larger when the $[Ca^{2+}]_{ext}$ was raised from 2 mM to 4 mM in KO (Fig. 5A,

313 top, see also Figure 6-figure supplement 1) and became more similar to those of WT. In Fig.
314 3, presynaptic recording showed that I_{Ca}s of WT at 1.5 mM $[Ca^{2+}]_{ext}$ were similar to those of
315 KO at 2 mM $[Ca^{2+}]_{ext}$. However, the WT EPSCs at 1.5 mM $[Ca^{2+}]_{ext}$ seemed larger than KO
316 at 2 mM $[Ca^{2+}]_{ext}$ (Fig. 5A, bottom, see also Figure 6-figure supplement 1). Changing the
317 $[Ca^{2+}]_{ext}$ from 1.5 mM to 2 mM in WT and from 2 mM to 4 mM in KO should have the same
318 potentiation effect on the EPSCs, if the reduced Ca^{2+} current amplitudes are the only
319 mechanism for reduced EPSCs in KO. In Fig. 5B, we calculated two types of potentiation
320 ratios: In WT, the ratio of the EPSC response in 2 mM to that in 1.5 mM $[Ca^{2+}]_{ext}$ was
321 calculated in each cell. In KO, the ratio of the EPSC response in 4 mM to that in 2 mM $[Ca^{2+}]_{ext}$
322 was calculated in each cell. When these two values were compared, the ratios were much
323 larger in KO (Fig. 5B, $p < 0.01$, t-test). Pr is more sensitive to the $[Ca^{2+}]_{ext}$ in the low end of
324 the dose-response curve because of the 3rd-4th power dependence of release on $[Ca^{2+}]_{ext}$ at
325 the low end (Dodge and Rahamimoff, 1967; Schneggenburger and Neher, 2000; Bollmann
326 et al., 2000). Therefore, the result suggests lower release probability in KO, even when the
327 amounts of Ca^{2+} influx were adjusted to be similar. When the paired pulse ratios were
328 compared, all four conditions (WT in 1.5 mM and 2 mM $[Ca^{2+}]_{ext}$, KO in 2 mM and 4 mM
329 $[Ca^{2+}]_{ext}$) provided similar values (Fig. 5C). The paired pulse ratio should be inversely
330 correlated to Pr, in principle. However, paired pulse facilitation in mossy fiber synapses could

331 be mediated by multiple effects, including Ca^{2+}-independent broadening of AP waveforms
332 (Geiger and Jonas, 2000) and Ca^{2+} buffer saturation which is more pronounced and
333 increases the paired-pulse ratios at higher $[Ca^{2+}]_{ext}$ (Blatow et al., 2003). Therefore, the value
334 might not be sensitive to the $[Ca^{2+}]_{ext}$.

335 We also analyzed the EPSCs in response to a stimulus train (50 Hz × 25 or 26
336 pulses) both in WT and KO (Fig. 6) under different external Ca^{2+} concentrations. When the
337 WT and KO responses were compared, the time course of facilitation/depression was quite
338 different between WT and KO (Fig. 6A-Fig. 6C). In 2 mM $[Ca^{2+}]_{ext}$, WT responses showed
339 initial facilitation (~2 fold) followed by depression, whereas KO responses showed
340 pronounced facilitation of ~10 fold. The difference could be due to both reduced Ca^{2+} currents
341 and impaired fusion competence in KO.

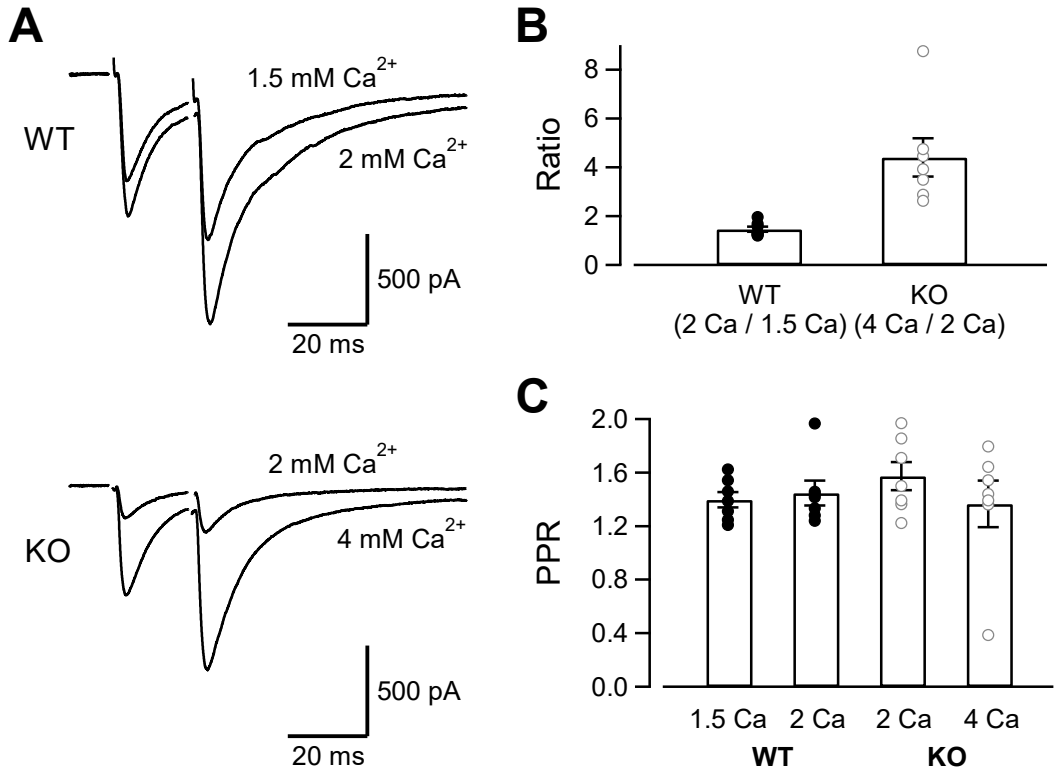

Figure 5. The evoked EPSC amplitudes in WT and KO, and their sensitivity to the extracellular Ca^{2+}

(**A**) The mossy fiber-evoked EPSCs measured at CA3 pyramidal cells. The fibers were stimulated twice with an interval of 20 ms. The responses of WT in 1.5 mM and 2 mM $[Ca^{2+}]_{ext}$ (n = 7 cells from 5 animals), as well as those of KO in 2 mM and 4 mM $[Ca^{2+}]_{ext}$ (n = 7 cells from 6 animals) are shown. The stimulus artifacts were blanked. (**B**) The amplitude ratios of WT EPSCs (2 mM / 1.5 mM $[Ca^{2+}]_{ext}$) and KO EPSCs (4 mM / 2 mM $[Ca^{2+}]_{ext}$) are shown. The concentrations were chosen to set the Ca^{2+} influx similar between WT and KO from Fig. 1-Fig. 3. (**C**) The paired pulse ratios under 4 conditions (WT in 1.5 mM and 2 mM $[Ca^{2+}]_{ext}$, KO in 2 mM and 4 mM $[Ca^{2+}]_{ext}$). Numerical values of plots are provided in Figure 5-source

353 data 1.

354 **Figure 5-source data 1.** Datasets of numerical values presented in Figure 5.

355

356 To adjust presynaptic Ca^{2+} influx to the similar level as the KO terminals, the $[Ca^{2+}]_{ext}$

357 was reduced to 1.5 mM in WT. Under this condition, presynaptic Ca^{2+} current amplitudes

358 were expected to be similar between WT and KO (in 2 mM $[Ca^{2+}]_{ext}$). If the reduced Ca^{2+}

359 influx is only responsible for smaller EPSCs in KO, we will observe similar time course of

360 train responses between WT and KO. However, facilitation was much less in the WT

361 condition (at 1.5 mM $[Ca^{2+}]_{ext}$, Fig. 6D, $p < 0.05$ from ANOVA), suggesting the mechanism

362 independent of Ca^{2+} influx. In order to obtain the same Ca^{2+} influx as that of WT in 2 mM

363 $[Ca^{2+}]_{ext}$, the $[Ca^{2+}]_{ext}$ was increased to 4 mM in KO. The time course of facilitation was

364 somewhat larger in the KO condition compared with that WT in 2 mM $[Ca^{2+}]_{ext}$. Because of

365 the data scatter in KO, the time course was statistically not significant ($p > 0.05$ from ANOVA).

366 Because multiple fibers were stimulated, the absolute EPSC amplitudes depend on not only

367 the release probability and the number of release sites per synapse, but also the number of

368 stimulated synapses. Nevertheless, when the absolute amplitudes were plotted against the

369 stimulus number, the differences were most prominent at the first responses in the train and

370 the differences were diminished later in the train, suggesting that the initial release probability

371 was likely to be lower at RIM-BP2 KO synapses, but the release could be restored during

372 repetitive stimulation (Figure 6-figure supplement 1). Restoration of release is consistent with

373 minor difference of capacitance changes in response to the depolarization (Figs. 1-4).

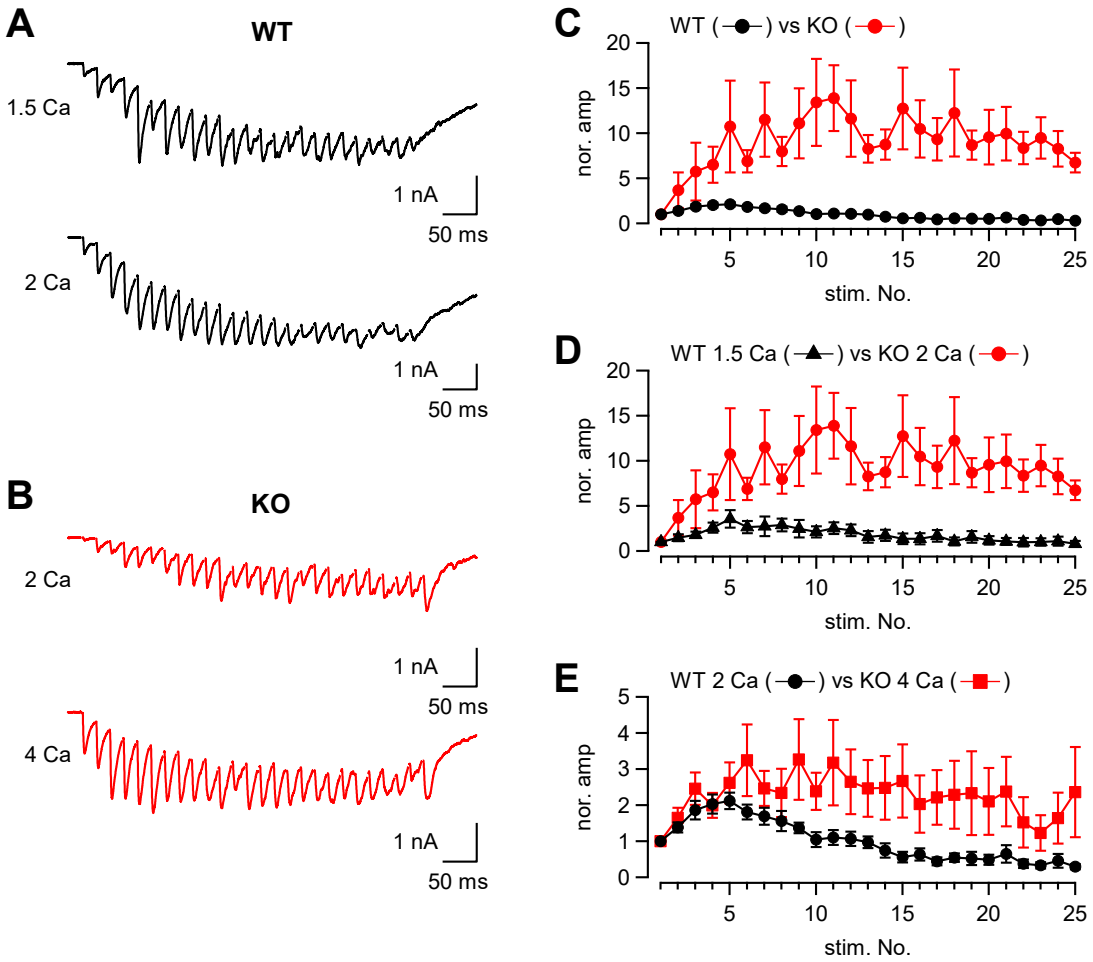

374

375 **Figure 6. The time course of synaptic facilitation/depression in WT and KO**

376 (**A**) Mossy fibers were stimulated at 50 Hz (25 times) and the evoked EPSCs were measured

377 in 1.5 mM (n = 5 cells from 4 animals) and 2 mM $[Ca^{2+}]_{ext}$ (n = 7 cells from 5 animals) in WT.

378 The stimulus artifacts were blanked. (**B**) Mossy fibers were stimulated at 50 Hz (26 times in

379 this particular example), and the evoked EPSCs were measured in 2 mM (n = 7 cells from 6

380 animals) and 4 mM $[Ca^{2+}]_{ext}$ (n = 8 cells from 6 animals). (**C**) The time course of EPSC

381 amplitudes during a 50 Hz train. The data were obtained from WT and KO in 2 mM $[Ca^{2+}]_{ext}$.

382 The time courses were significantly different ($p < 0.01$ from ANOVA). (**D**) The same as (**C**),

383 but the data were obtained from WT in 1.5 mM $[Ca^{2+}]_{ext}$ and KO in 2 mM $[Ca^{2+}]_{ext}$. The time

384 courses were significantly different ($p < 0.05$ from ANOVA). (**E**) The same as (**C**), but the data

385 were obtained from WT in 2 mM $[Ca^{2+}]_{ext}$ and KO in 4 mM $[Ca^{2+}]_{ext}$. Numerical values of plots

386 are provided in Figure 6-source data 1. The time courses were not significantly different ($p =$

387 0.12 from ANOVA). Numerical values of plots are provided in Figure 6-source data 1.

388

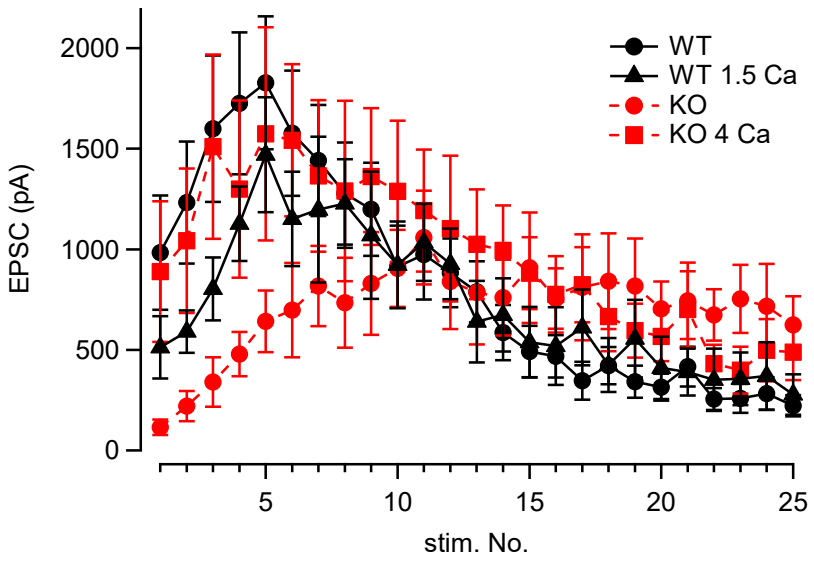

389

390 **Figure 6-figure supplement 1. The EPSC amplitudes plotted against the stimulus**

391 **number**

392 The same data sets as Fig. 6C-Fig. 6E, but the absolute EPSC amplitudes are plotted instead

of the normalized amplitudes. Numerical values of plots are provided in Figure 6-source data 1. Raw data were summarized. In Fig. 5 and Fig. 6, the effect of holding potential was corrected so that the values were adjusted to those at -70 mV. Numerical values of plots are provided in Figure 6-source data 1.

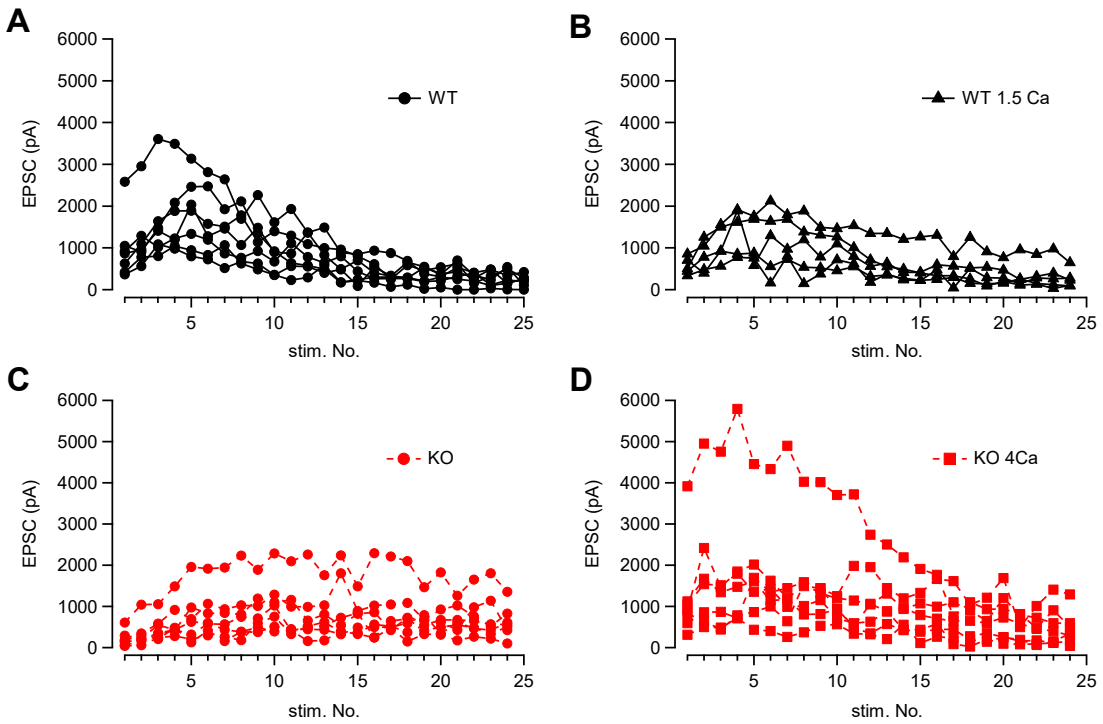

Figure 6-figure supplement 2. The individual data of Fig. 6

WT in 2mM (**A**) and 1.5 mM (**B**) $[Ca^{2+}]_{ext}$, and KO in 2 mM (**C**) and 4 mM $[Ca^{2+}]_{ext}$ (**D**) are shown. Numerical values of plots are provided in Figure 6-source data 1.

Figure 6-source data 1. Datasets of numerical values presented in Figure 6, Figure 6-figure supplement 1, and Figure 6-figure supplement 2.

404 **STED microscopy is consistent with less abundance of P/Q-type Ca^{2+} channels in RIM-**

405 **BP2 KO.**

406 Our electrophysiological data suggest that RIM-BP2 may regulate the abundance

407 of Ca^{2+} channels. In order to directly study the Ca^{2+} channel abundance at the AZ, we

408 performed STED microscopy analysis of Ca^{2+} channels in WT and RIM-BP2 KO hippocampal

409 mossy fiber terminals. We here focused on P/Q-type and N-type Ca^{2+} channels because both

410 Ca^{2+} channel types are relevant for transmitter release at this synapse (Castillo et al., 1994;

411 Pelkey et al., 2006; Li et al., 2007). We performed immunohistochemistry on thin brain

412 cryosections from WT and RIM-BP2 KO mice. STED microscopy confirmed complete loss of

413 RIM-BP2 proteins in KO terminals (Figure 7-figure supplement 1). We then

414 immunohistochemically labeled the α-subunit of either P/Q-type Ca^{2+} channel (Cav2.1) or N-

415 type Ca^{2+} channel (Cav2.2) and Munc13-1 (AZ/release site marker, Böhme et al., 2016;

416 Sakamoto et al., 2018) with VGLUT1 (presynaptic marker) and PSD-95 (postsynaptic

417 marker) (Fig. 7A, Fig. 7B and Figure 7-figure supplement 2). In the stratum lucidum of the

418 hippocampal CA3 region, mossy fibers form large synapses containing multiple and clustered

419 AZs on CA3 pyramidal cells, and also small en passant and filopodial synapses containing a

420 single AZ on interneurons (Acsády et al., 1998; Rollenhagen et al., 2007). Consistent with

421 this, large VGLUT1 positive terminals rarely contacted interneurons marked with two major

422 interneuron markers, mGluR1α and GluA4 (Figure 7-figure supplement 3). Thus, we
423 identified AZs using Munc13-1 STED images and quantified the signal intensity of Cav2.1 or
424 Cav2.2 only at AZs clustered in large VGLUT1 positive terminals in the CA3 stratum lucidum,
425 allowing us to confine the analysis to large mossy fiber terminals innervating onto CA3
426 pyramidal cells. The total signal intensity of Cav2.1 at the AZ was 22% lower in RIM-BP2 KO
427 mice (n = 4 animals) than in WT mice (n = 4 animals) (p = 0.0286) (Fig. 7C, left). These data
428 are consistent with the reduction of Ca^{2+} currents in RIM-BP2 KO mice (Fig. 1), though STED
429 microscopy is non-linear and can only provide qualitative differences regarding intensity. In
430 addition, the spatial resolution of STED microscopy (especially z axis) does not assign the
431 signals to the large mossy fiber terminal rigidly. The area, length, and width of Cav2.1 clusters
432 in the AZ were not different between WT and RIM-BP2 KO terminals (Figure 7-figure
433 supplement 4). The analysis in this study might not have spatial resolution to detect the
434 differences. The analysis from the confocal microscopy also indicated that the signal intensity
435 of Cav2.1 was reduced in KO, consistent with the STED data (Figure 7-fugure supplement
436 5).

437 In contrast to Cav2.1, the total signal intensity of Cav2.2 and Munc13-1 did not
438 significantly differ between WT and RIM-BP2 KOs (p = 0.3143 and p = 0.0831) (Fig. 7C,
439 right), though it remains possible that we failed to detect some changes. Furthermore, we

440 found that the number of Cav2.1 clusters within the AZ identified by STED deconvolution
441 analysis was not altered (2.5 ± 0.11 in WT, n = 4 animals; 2.3 ± 0.02 in KO, n = 4 animals) (p
442 = 0.114). These data are consistent with the idea that RIM-BP2 KO reduces the abundance
443 of P/Q-type Ca^{2+} channels per cluster. To optically estimate physical distances between Ca^{2+}
444 channels and release sites, we next analyzed the nearest neighboring distance between
445 Cav2.1 and Munc13-1 clusters. These distances were unchanged (61 ± 1.4 nm in WT, n = 4
446 animals; 64 ± 1.3 nm in KO, n = 4 animals) (p = 0.200) (Fig. 7D), consistent with the similar
447 sensitivity of release to EGTA between WT and RIM-BP2 KO mice. However, the resolution
448 of STED microscopy cannot allow detection of small differences of the cluster number and
449 the distance between WT and KO. From these results together with presynaptic recordings,
450 we suggest that decreased Ca^{2+} influx in RIM-BP2 KO hippocampal mossy fiber terminals is
451 caused by less abundance of P/Q-type Ca^{2+} channels at the AZ.

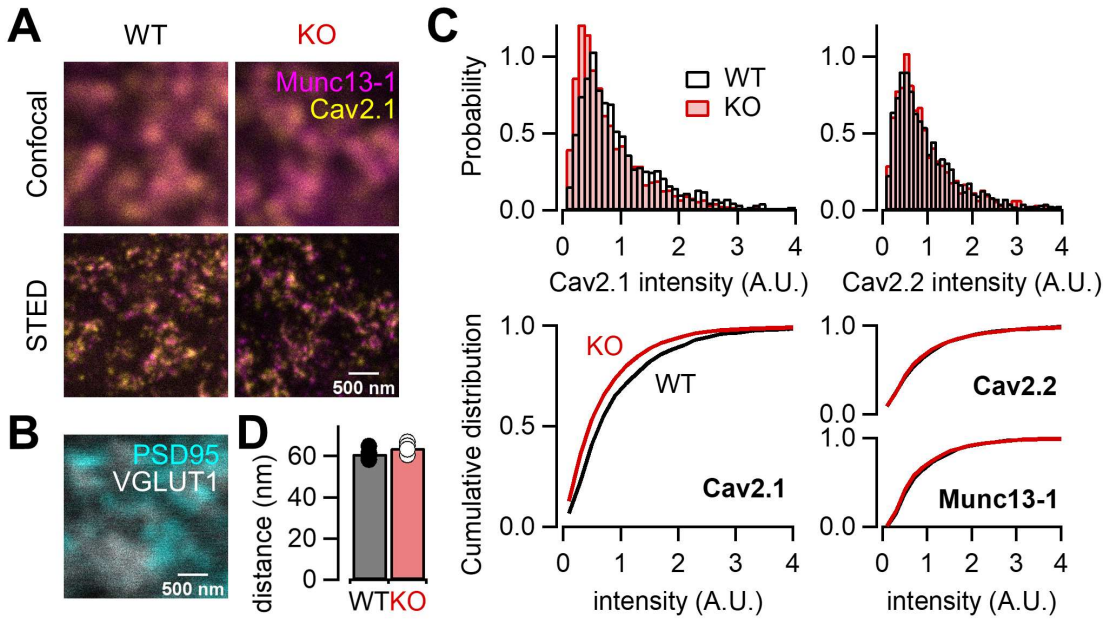

452

453 **Figure 7. RIM-BP2 deletion alters the signal intensity of Cav2.1 clusters within the AZ**

454 (**A**) Confocal *(top)* and STED *(bottom)* images of Munc13-1 (magenta) and Cav2.1 (yellow)

455 clusters at hippocampal mossy fiber terminals of WT *(left)* and RIM-BP2 KO *(right)* mice.

456 (Scale bar: 500 nm.) (**B**) Confocal images of PSD95 (cyan) and VGLUT1 (white) to identify

457 glutamatergic synapses in CA3 stratum lucidum: mossy fiber-CA3 synapses. (Scale bar: 500

458 nm.) The image was taken from same region shown in (**A**), *(left)*. (**C**) Histograms *(top)* and

459 cumulative distribution plots *(bottom)* of the total signal intensity of Cav2.1 *(left)*, Cav2.2, and

460 Munc13-1 *(right)* at AZs in WT (black) and RIM-BP2 KO (red) mice. (**D**) The average nearest

461 neighbor distance between Cav2.1 and Munc13-1 clusters in WT (black; n = 4 animals) and

462 RIM-BP2 KO (red; n = 4 animals) mice. Several hundreds of AZs per image were analyzed.

463 Data show the average value of distance per animal and error bars represent SEM. Each

464 data point indicates individual values. Numerical values of plots are provided in Figure 7-

465 source data 1.

466 **Figure 7-source data 1.** Datasets of numerical values presented in Figure 7.

467

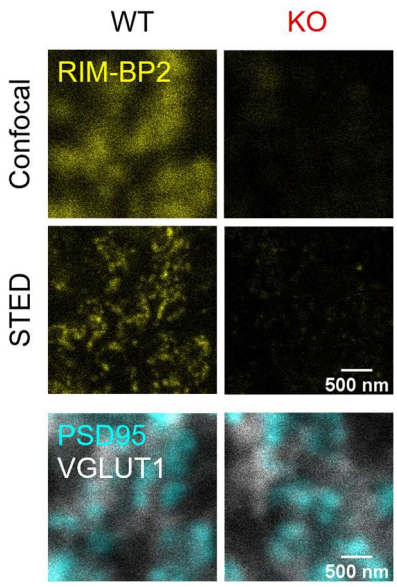

468

469 **Figure 7-figure supplement 1. STED microscopy confirmed loss of RIM-BP2 proteins**

470 **in KO terminals**

471 Confocal *(top)* and STED *(middle)* images of RIM-BP2 (yellow) in WT *(left)* and RIM-BP2 KO

472 *(right)* hippocampal mossy fiber terminals identified by PSD95 (cyan) and VGLUT1 (white)

473 *(bottom)*. (Scale bar: 500 nm.) The *bottom* images show the same region as *top* and *middle*.

474

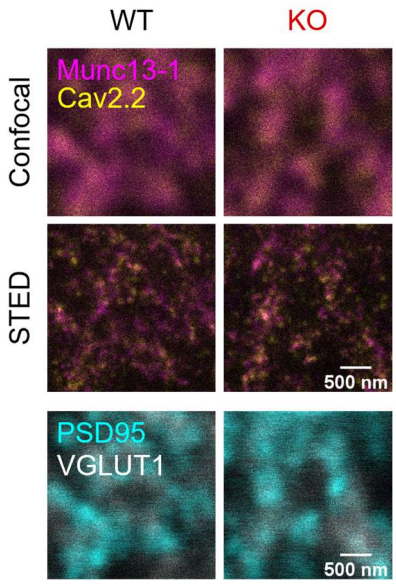

Figure 7-figure supplement 2. STED imaging of Cav2.2 at hippocampal mossy fiber terminals

Confocal *(top)* and STED *(middle)* images of Munc13-1 (magenta) and Cav2.2 (yellow) clusters in WT *(left)* and RIM-BP2 KO *(right)* mice. Confocal images of PSD95 (cyan) and VGLUT1 (white) in the same region as *top* and *middle* are also shown *(bottom)*. (Scale bar: 500 nm.)

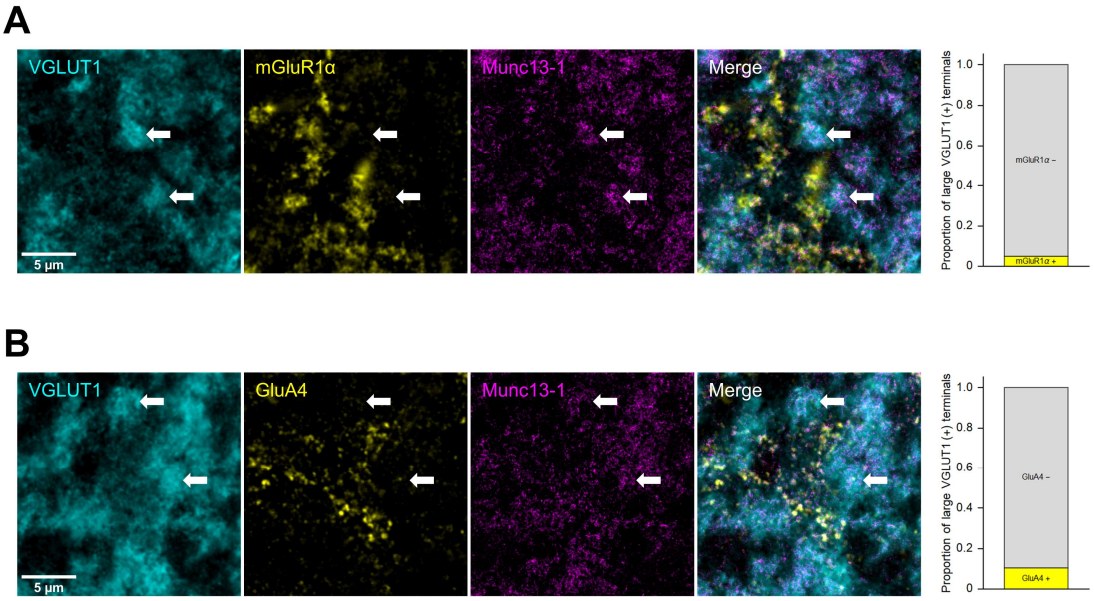

Figure 7-figure supplement 3. Immunohistochemical characterization of large VGLUT1 positive terminals in the CA3 stratum lucidum

(**A**) Confocal images of VGLUT1 (cyan) and mGluR1α (yellow) were taken with STED images of Munc13-1 (magenta) in the CA3 stratum lucidum. Arrows indicate representative large MF terminals identified by VGLUT1 signals (Scale bar: 5 μm.) The right graph shows the proportion of large VGLUT1 positive terminals contacting mGluR1α positive processes. (**B**) Same as (**A**) but for GluA4 instead of mGluR1α. (Scale bar: 5 μm.)

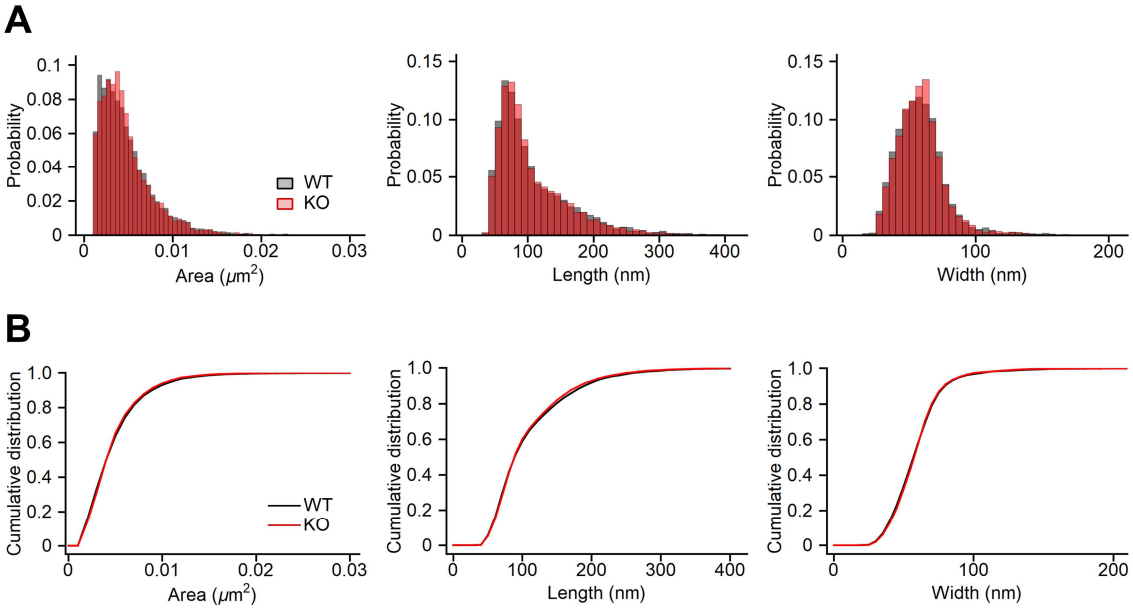

Figure 7-figure supplement 4. The area, length, width of Cav2.1 cluster

In A, distribution plots of area (left), length (middle) and width (right) are shown. In B, cumulative distribution plots are shown. The same samples as Fig. 7. Numerical values of plots are provided in Figure 7-figure supplement 4-source data 1.

Figure 7-figure supplement 4-source data 1. Datasets of numerical values presented in Figure 7-figure supplement 4.

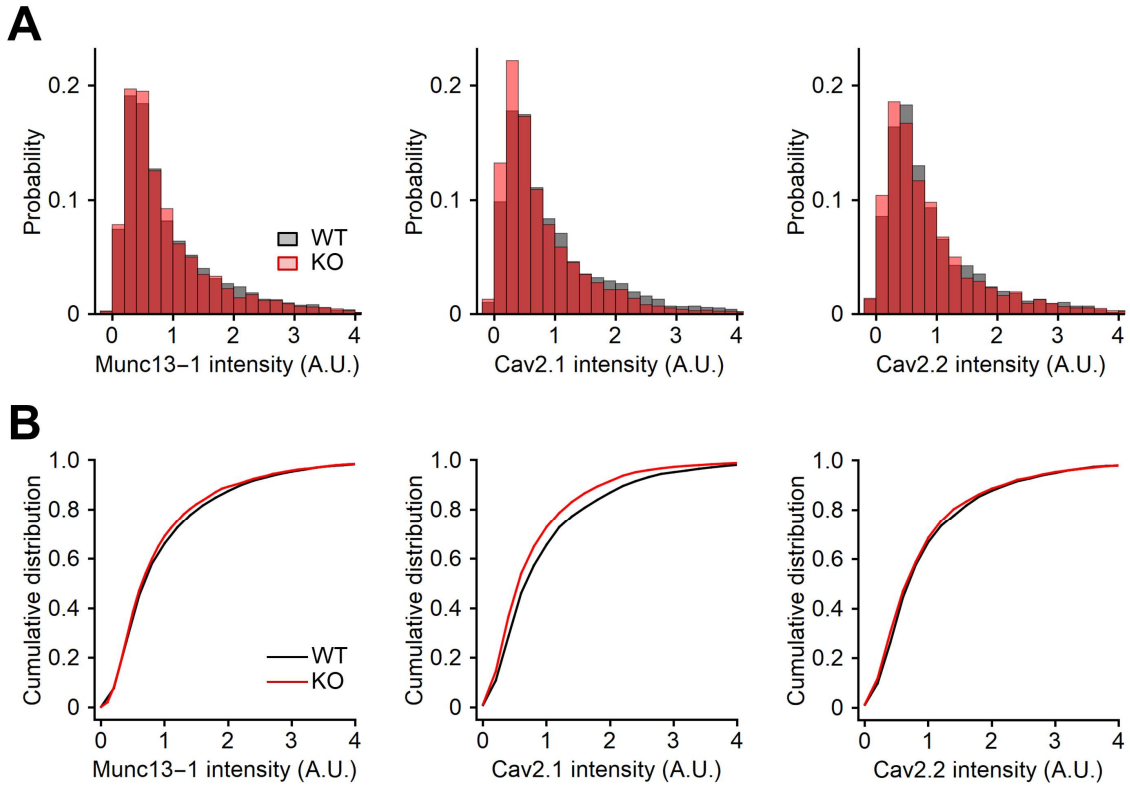

Figure 7-figure supplement 5. Quantification of the signal intensity using confocal images

The signal intensity of Munc13-1 *(left)*, Cav2.1 *(middle)*, and Cav2.2 *(right)* at AZs in WT (black) and RIM-BP2 KO (red) mice were quantified from confocal images. The position of AZ was determined from the Munc13-1 STED data, and the signal intensity of Munc13-1, Cav2.1 and Cav2.2 was measured. Histograms (**A**) and cumulative distribution plots (**B**) are shown. The same samples as Fig. 7. Numerical values of plots are provided in Figure 7-figure supplement 5-source data 1.

Figure 7-figure supplement 5-source data 1. Datasets of numerical values presented in Figure 7-figure supplement 5.

511

512 **Discussion**

513 Accumulation of Ca^{2+} channels at the AZ, and efficient vesicle docking and priming
514 are essential factors for fast synaptic vesicle exocytosis. AZ proteins are critical for fast
515 synchronous release and synaptic diversity. RIM-BPs have been implicated in recruitment of
516 Ca^{2+} channels to the AZ (Kaeser et al., 2011; Liu et al., 2011) by interacting with RIMs and
517 Ca^{2+} channels (Wang et al., 2000; Hibino et al., 2002). In addition, RIM-BPs, like RIM1/2,
518 recruit Munc-13 and accelerate synaptic vesicle priming (Brockmann et al., 2020). At murine
519 central synapses, RIM-BPs deficient synapses demonstrate overall a rather mild decrease
520 in the amounts of transmitter release (Acuna et al., 2015; Grauel et al., 2016; Luo et al., 2017;
521 Krinner et al., 2017; Brockmann et al., 2019; Butola et al., 2021). Most studies so far have
522 been mainly focused on synapses with high release probability (phasic synapses) such as
523 the calyx of Held and CA3-CA1 synapses. That said, at mossy fiber-CA3 synapses, KO of
524 RIM-BPs has a strong influence on synaptic transmission (Brockmann et al., 2019). Notably,
525 at mossy fiber-CA3 synapses, release probability is relatively low (tonic synapses). It was
526 unknown whether the reduction of transmitter release at RIM-BP2 KO mossy fiber synapses
527 was due to impaired Ca^{2+} channel recruitment, and / or impaired vesicle docking or priming.
528 Using STED microscopy, Brockmann et al. (2019) suggested that the physical recruitment of

529 Munc13-1 might be an important function of RIM-BP2, though functional demonstration had
530 been lacking.

531 By using direct presynaptic patch clamp recordings, we here observed a decrease
532 of Ca^{2+} current amplitudes (~30%) in RIM-BP2 KO mice (Fig. 1). Consistently, STED
533 microscopy supported reduced abundance of P/Q-type Ca^{2+} channels (Cav2.1) in the mutant
534 mossy fiber terminal (Fig. 7). Interestingly, this observation is similar to that at Drosophila
535 NMJ and hair cell synapses (Liu et al., 2011; Krinner et al., 2017), but not that at other
536 synapses (Acuna et al., 2015; Grauel et al., 2016; Butola et al., 2021), suggesting that the
537 functional role of RIM-BP2 in recruiting Ca^{2+} channels differs among synapse types.

538 Brockmann et al. (2019) observed a reduction of Munc13-1 cluster number and
539 docked vesicles in RIM-BP2 deficient synapses at hippocampal mossy fiber terminals (Fig.
540 7). They identified the terminals by using ZnT3, enriched at mossy fiber (Brockmann et al.,
541 2019; Wenzel et al., 1997). Our STED imaging did not detect differences in Munc13-1 cluster
542 number at the AZ between WT and RIM-BP2 KO mice. Notably, we analyzed the number of
543 Cav2.1, Cav2.2 and Munc13-1 clusters only within AZs showing direct co-localization with
544 VGLUT1 and PSD-95, which mainly reflects the AZs facing CA3 pyramidal cells rather than
545 the synapses onto interneurons (Acsády et al., 1998; Rollenhagen et al., 2007). Such a
546 difference in areas analyzed between previous and our study might explain the difference. In

547 addition, some developmental variability/compensation could still occur in the range we
548 studied and be relevant for the discrepancy between Munc13-1 results between Brockmann
549 et al. (2019) and this study. Also, the spatial resolution of our study is limited and we cannot
550 rigidly measure the signals only from large mossy fiber terminals. It is important to state that
551 our results do not exclude roles of RIM-BP2 in synaptic vesicle priming. Indeed, we have
552 shown that the reduction of the EPSC amplitudes could not be fully explained by the reduced
553 Ca^{2+} influx (Fig. 5). Because the differences in the RRP size measured from capacitance
554 measurements were relatively minor (Fig. 1-Fig. 3), the fusion competence was likely to be
555 impaired by RIM-BP2 KO, but this could be overcome by large Ca^{2+} influx. Consistently, the
556 EPSCs responses of KO became larger and comparable to those of WT (Fig. 6A, Fig. 6B,
557 and Figure 6-figure supplement 1) during repetitive AP stimulation, at least qualitatively.

558 Recent studies have reported that RIM-BPs deletion altered Ca^{2+} channel
559 localization and loosened the coupling between Ca^{2+} channels and synaptic vesicles at
560 mammalian synapses (Acuna et al., 2015; Grauel et al., 2016; Butola et al., 2021). We
561 investigated the Ca^{2+} channel-vesicle coupling at hippocampal mossy fiber terminals. The
562 sensitivity of release to Ca^{2+} chelator EGTA was not changed between WT and RIM-BP2 KO
563 mice. We also indicated RIM-BP2 KO did not alter the coupling of Ca^{2+} channels to release
564 sites by using STED microscopy, though spatial resolution of STED microscopy in this study

565 could not allow to detect small changes (Fig. 7) .

566 At some mammalian synapses, deletion of RIM-BP2 affects physical distance
567 between Ca^{2+} channels and synaptic vesicles (Acuna et al., 2015; Grauel et al., 2016; Butola
568 et al., 2021). In contrast, at hippocampal mossy fiber terminals having low release probability
569 (Vyleta and Jonas, 2014), RIM-BP2 KO decreased the abundance of P/Q-type Ca^{2+} channels,
570 thereby reducing Ca^{2+} influx and neurotransmitter release. We hypothesize the specific
571 molecular-architectural and biochemical contributions by RIM-BPs might be of different
572 relevance among different types of synapses. Brockmann et al. (2020) proposed that RIM-
573 BP2 controlled Ca^{2+} channel recruitment and vesicle priming by profound interaction with
574 RIMs and Munc13s. These results have been obtained through studying hippocampal
575 cultures dominated by phasic synapses. It seems possible that the interaction among three
576 protein types is tight at some types of phasic synapses, simply because of high density of
577 these proteins at AZs. Alternatively, one might speculate about additional proteins, different
578 interaction surfaces taken, transsynaptic columns (Tang et al., 2016). Deletion of RIM-BP2
579 does not lead to loss of Ca^{2+} channels themselves and/or vesicle priming due to remaining
580 RIMs, Munc13, and other proteins, which can regulate recruitment of Ca^{2+} channels and
581 synaptic vesicle priming without RIM-BP2. Instead, fine-tuning of release such as
582 synchronization is compromised. We hypothesize that AZ scaffold might be differently built,

583 leading to different consequences when eliminating one component. Hence deletion of RIM-
584 BP2 leads to immediate loss of Ca^{2+} channels and vesicle priming. This is in line with the
585 proposal that at hippocampal mossy fiber synapses, synaptic vesicles are only loosely
586 coupled with Ca^{2+} channels (Vyleta and Jonas, 2014) and vesicles are de-primed under
587 resting conditions (Miki et al., 2016; Neher and Brose, 2018). Future research along this line
588 may lead to an understanding of how fine molecular differences in the AZ scaffolds might
589 orchestrate synaptic diversity.

590 Although this study reveals reduction of Ca^{2+} currents and reduced fusion
591 competence in RIM-BP2 KO mossy fiber synapses, it has some limitation. Most importantly,
592 with conventional knockouts the observed changes could reflect compensatory
593 developmental changes and not direct outcomes of the RIM-BP2 knockout. This issue should
594 be resolved by using region-specific and time-dependent conditional KO.

595

596 **Materials and Methods**

597 **Slice preparation**

598 All animal experiments were conducted in accordance with the guidelines of the
599 Physiological Society of Japan, and were approved by Doshisha University Animal
600 Experiment Committee (A22063, D22063).

601 We used male and female C57BL/6 mice (postnatal days 35-40). WT and RIM-BP2
602 KO mice (Grauel et al., 2016) were deeply anesthetized with isoflurane and decapitated.
603 Their brains were quickly removed and chilled in sherbet-like cutting solution containing (in
604 mM): 87 NaCl, 75 sucrose, 25 $NaHCO_3$, 1.25 NaH_2PO_4, 2.5 KCl, 10 glucose, 0.5 $CaCl_2$ and
605 7 $MgCl_2$ bubbled with 95% O_2 and 5% CO_2 (Hallermann et al., 2003). Hippocampal slices
606 (300 μm thick) were prepared from brains using a vibratome (VT1200S, Leica) in ice-cold
607 cutting solution. After slicing, slices were incubated in cutting solution at 37°C for 30 min, and
608 subsequently kept at room temperature (22-25°C) up to 4 h.
609
610 **Whole-cell recordings**
611 Electrophysiological recordings were performed in a recording chamber filled with
612 the extracellular solution containing (in mM): 125 NaCl, 2.5 KCl, 25 glucose, 25 $NaHCO_3$,
613 1.25 NaH_2PO_4, 0.4 ascorbic acid, 3 myo-inositol, 2 Na-pyruvate, 2 $CaCl_2$ and 1 $MgCl_2$
614 saturated with 95% O_2 and 5% CO_2. In some experiments, the concentration of $CaCl_2$ was
615 changed to 1 mM, 1.5 mM and 4 mM. For presynaptic membrane capacitance
616 measurements, 1 μM tetrodotoxin (TTX, Wako) was added to block Na^+ channels.
617 Moreover, for recording Ca^{2+} currents (Fig. 1B), 10 mM TEA-Cl was added to block K^+
618 channels. Slices were visualized by an upright microscope (BX-51, Olympus). Whole-cell

619 patch-clamp recordings were applied to hippocampal mossy fiber terminals and CA3
620 pyramidal cells at room temperature. The patch pipettes were filled with the intracellular
621 solution containing (in mM): 135 Cs-gluconate, 20 TEA-Cl, 10 Hepes, 5 Na_2-
622 phosphocreatine, 4 MgATP, 0.3 GTP and 0.5 EGTA (pH = 7.2 adjusted with CsOH). In
623 some experiments, the concentration of EGTA was changed to 5 mM. Presynaptic patch
624 pipettes (BF150-86-10, Sutter Instrument) had a resistance of 15-20 MΩ and series
625 resistance (R_s) was 30-70 MΩ. R_s was compensated so that residual resistance was 30-35
626 MΩ. For postsynaptic recordings, the same internal solution was used, except that EGTA
627 concentration was raised to 5 mM. Postsynaptic patch pipettes (BF150-86-10, Sutter
628 Instrument) had a resistance of 3-7 MΩ and series resistance (R_s) was 5-20 MΩ which was
629 compensated by 50-80 %.

630 Patch-clamp recordings were performed using an EPC10/3 or EPC10/2 amplifier
631 (HEKA) in voltage-clamp mode, controlled by Patchmaster software (HEKA). Membrane
632 currents were low-pass filtered at 2.9 kHz and sampled at 20 or 50 kHz.

633 Membrane capacitance measurements were performed using an EPC10/3
634 amplifier in the sine + DC configuration (Gillis, 2000) using Patchmaster software (HEKA). A
635 sine wave (30 mV in amplitude, 1000 Hz in frequency) was superimposed on the holding
636 potential of -80 mV. The terminal was depolarized from -80 mV to +10 mV for 5-100 ms.

637 The IV of presynaptic Ca currents were measured by sequential depolarized for 5 ms, with
638 2 ms intervals from -80 mV to +70 mV by 10 mV steps.
639 For the EPSC measurements, postsynaptic cells (CA3 pyramidal cells) were
640 voltage clamped at -60 - -80 mV. For Figs. 5 and 6, the data were corrected for the different
641 holding potential (re-calculated to the value at -70 mV assuming the reversal potential of 0
642 mV, which may have the correction effect of ~15 %). At the end of the experiments, DCG-Ⅳ
643 was applied to confirm mossy fiber synaptic responses, whenever possible. The mossy
644 fibers were stimulated extracellularly using a glass electrode used for patch clamp
645 containing the extracellular solution and the stimulation intensity was usually 10-60 V.
646 Data were obtained from at least three different WT and RIM-BP2 KO terminals in
647 each set of experiments (biological replicate).
648
649 **Immunostaining**
650 Brains of WT and RIM-BP2 KO mice were quickly removed and transferred to
651 cryomold (Sakura Finetek) filled with tissue freezing medium (Leica). Brains were
652 instantaneously frozen on aluminum block in liquid nitrogen and stored at -80°C. For
653 cryosectioning, frozen brains were kept in cryostat (CM1860, Leica) at -18°C for 30 min.
654 Then, 10 μm-thick sections were sliced and collected on cover glasses (Matsunami glass,

655 25×25 No.1). Sections were quickly fixed by dehydration with a heat blower at 50°C for 1
656 min, and further dehydrated in ethanol for 30 min at -25°C and in acetone for 10 min on ice.
657 After blocking with PBS containing 0.3% BSA at room temperature, sections were
658 incubated with primary antibodies diluted in PBS containing 0.3% BSA: anti-VGLUT1
659 (1:2000, Synaptic Systems, guinea pig polyclonal, RRID:AB_887878), anti-PSD-95 (1:50,
660 NeuroMab, mouse monoclonal IgG2a, clone K28/43, TC Supernatant, RRID:AB_2877189),
661 anti-Munc13-1 (1:1000, mouse monoclonal IgG1, clone 11B-10G, Sakamoto et al., 2018),
662 and anti-Cav2.1 (1:400, Synaptic Systems, rabbit polyclonal, RRID:AB_2619841) or anti-
663 Cav2.2 (1:400, Synaptic Systems, mouse monoclonal IgG2b, clone 163E3,
664 RRID:AB_2619843) or anti-RIM-BP2 (1:200, mouse monoclonal IgG2b, clone 8-4G,
665 Sakamoto et al., 2022) for 3 hours at room temperature. Afterwards, sections were washed
666 and incubated with fluorescence dye labeled secondary antibodies: DyLight 405 Anti-
667 Guinea Pig IgG (Jackson ImmunoResearch, RRID:AB_2340470), Alexa Fluor 488 (Thermo
668 Fisher Scientific) labeled Anti-Mouse IgG2a (Jackson ImmunoResearch,
669 RRID:AB_2338462), STAR635P (Abberior) labeled Anti-Mouse IgG1 (Jackson
670 ImmunoResearch, RRID:AB_2338461), and Alexa Fluor 594 (Thermo Fisher Scientific)
671 labeled Anti-Rabbit IgG (Jackson ImmunoResearch, RRID:AB_2340585) or Anti-Mouse
672 IgG2b (Jackson ImmunoResearch, RRID:AB_2338463) for 1 hour at room temperature.

673 Sections were post-fixed with 4% PFA in PBS and washed with PBS. Sections were
674 mounted on coverslips using Prolong Glass Antifade Mountant (Thermo Fisher Scientific).
675 The same number of sections were obtained from WT and RIM-BP2 KO brains and
676 processed in parallel at the same experimental day (biological replicate).
677 For Figure 7-figure supplement 3, only WT brains were used. Primary antibodies
678 used were anti-VGLUT1 (1:2000, Synaptic Systems, rabbit polyclonal, RRID:AB_887877),
679 anti-VGLUT1 (1:2000, Synaptic Systems, guinea pig polyclonal, RRID:AB_887878), anti-
680 mGluR1α (1:200, Nittobo Medical, guinea pig polyclonal, mGluR1a-GP-Af660), anti-
681 GluA4C (1:100, Nittobo Medical, rabbit polyclonal, GluR4C-Rb-Af160), and anti-Munc13-1
682 (1:1000, mouse monoclonal IgG1, clone 11B-10G).
683
684 **STED imaging**
685 STED imaging was performed using TCS SP8 STED 3x microscope (Leica)
686 equipped with a 405 nm diode laser, a pulsed white light laser (WLL), a continuous 592 nm
687 STED laser for alignment, a pulsed 775 nm STED laser, HyD detectors, and a 100× oil-
688 immersion objective lens (NA = 1.4). STED images were acquired using the Leica LAS-X
689 software with an image format of 1024×1024 pixels, 16-bit sampling, 8-line accumulations,
690 and 11.36-zoom factor, yielding a pixel size of 10 nm. HyD detectors were configured to

691 counting mode with a gating from 0.5 to 6.5 nanosecond. A 405 nm diode laser was used to
692 excite DyLight405. Alexa488, Alexa594, and STAR635P were excited using WLL at 488
693 nm, 561 nm, and 633 nm, respectively. The 775 nm STED laser power was set to 75% and
694 100% of maximum power for depletion of STAR635P and Alexa594, respectively, and delay
695 time was set to 300 picoseconds. STED imaging was performed on thin sections obtained
696 from four different WT and RIM-BP2 KO mice (biological replicate). Images were acquired
697 three times from each section (technical replicate).
698
699 **Analysis**
700 For electrophysiological experiments, the data were analyzed by Igor Pro
701 (WaveMetrics) or Excel (Microsoft Corp). Presynaptic calcium currents were measured at
702 the peak amplitude during the depolarizing pulse. Capacitance jumps were measured
703 between baseline (before the pulse) and ~10 ms after the pulse where the effect of tail
704 currents became minor. To determine the time constant of release, an exponential fit was
705 applied. Values are given as mean ± SEM, and n indicates the number of recorded
706 terminals or the number of animals used. Statistical method of sample size determination
707 was not done, but our sample sizes are similar to those of previous studies (Hallermann et
708 al., 2003, Midorikawa and Sakaba, 2017).

709 For STED imaging, data were analyzed using custom-designed programs in
710 Mathematica (Wolfram), values were processed by Igor Pro (WaveMetrics), and pictures
711 were created with ImageJ (NIH). To determine the area of AZs, image masks were
712 generated from STED images of Munc13-1 by unsharp masking and image binarization.
713 Only AZs that show co-localization with VGLUT1 and PSD-95 immunofluorescence signals
714 were included in the analysis. To confine the analysis to the large mossy fiber boutons, AZs
715 in presynaptic terminals of small VGLUT1-positive area were excluded. Then, the
716 background subtracted integral of signal intensity of Cav2.1 or Cav2.2 was quantified using
717 the image masks of AZs. The background signal intensity was estimated from non-AZ area
718 in the same STED images. For quantification of Cav2.1 clusters in the AZs, STED images
719 of Cav2.1 were deconvolved using a gaussian kernel with a radius of 40 nm. Image masks
720 of each Ca^{2+} channel were generated from deconvolved STED images by unsharp masking
721 and image binarization. Then, the total signal intensity, the size, and the number of Cav2.1
722 clusters at the AZs were quantified using the image masks of Cav2.1 clusters. Custom-
723 designed programs in Mathematica (Wolfram) are available from Source code 1. Values
724 are given as mean ± SEM, and n indicates the number of animals. Statistical method of
725 sample size determination was not done, but our sample sizes are similar to those of
726 previous studies (Brockmann et al., 2019).

727 Experiments were not fully randomized and blinded.

728 Statistical analysis was done in MATLAB (The MathWorks) or SPSS (IBM). t-test,
729 ANOVA, and mixed model were used for statistical tests. Significance level was set at α =
730 0.05, and p values were described in the main text or figure legends.

731

732 **Data availability**

733 All data generated in this study are included in the main text or shown as scatter
734 plots in each graph. Numerical values of graphs are provided in Source data files. The
735 custom-written code files in Mathematica are uploaded as Source code file.

736

737 **Acknowledgements**

738 We thank Stephan Sigrist, Dietmar Schmitz and Christian Rosenmund for kindly
739 providing us RIM-BP2 KO mice. We also thank Stephan Sigrist for comments on the
740 manuscript and The IRCN Imaging Core, The University of Tokyo Institutes for Advanced
741 Studies, for the use of STED microscopy and for assistance. This works has been supported
742 by JSPS KAKENHI (JP20J20550 to RM, JP20KK0171, JP21K15183 to HS, JP20H03427 to
743 KH, JP20KK0171, JP21H02598 to TS), JSPS Core-to-Core program A. Advanced Research
744 Networks (JPJSCCA20220007 to TS), JST PRESTO (JPMJPR21E7 to HS) and Takeda

Science Foundation (Bioscience and Specific Research Grants to TS).

Competing interests

None

Additional information

Author ORCIDs

Rinako Miyano https://orcid.org/0000-0002-0022-7198

Hirokazu Sakamoto https://orcid.org/0000-0002-9881-5173

Kenzo Hirose https://orcid.org/0000-0002-8944-6513

Takeshi Sakaba https://orcid.org/0000-0003-0688-7717

757 **References**

758 Acsády L, Kamondi A, Sík A, Freund T, Buzsáki G. 1998. GABAergic cells are the major
759 postsynaptic targets of mossy fibers in the rat hippocampus. *Journal of Neuroscience*
760 **18**:3386-3403. DOI: https://doi.org/10.1523/JNEUROSCI.18-09-03386.1998, PMID:
761 9547246

762 Acuna C, Liu X, Gonzalez A, Südhof TC. 2015. RIM-BPs Mediate Tight Coupling of
763 Action Potentials to Ca^{2+}-Triggered Neurotransmitter Release. *Neuron* **87**:1234-1247.
764 DOI: https://doi.org/10.1016/j.neuron.2015.08.027, PMID: 26402606

765 Adler EM, Augustine GJ, Duffy SN, Charlton MP. 1991. Alien intracellular calcium
766 chelators attenuate neurotransmitter release at the squid giant synapse. *Journal of*
767 *Neuroscience* **11**:1496-1507. DOI: https://doi.org/10.1523/JNEUROSCI.11-06-
768 01496.1991, PMID: 1675264

769 Blatow M, Caputi A, Burnashev N, Monyer H, Rozov A. 2003. Ca^{2+} buffer saturation
770 underlies paired pulse facilitation in calbindin-D28k-containing terminals. *Neuron* **38**: 79-
771 88. DOI: https://doi.org/10.1016/s0896-6273(03)00196-x, PMID: 12691666

772 Bollmann JH, Sakmann B, Borst JG. 2000. Calcium sensitivity of glutamate release in a
773 calyx-type terminal. *Science* **289**: 953-957. DOI:
774 https://doi.org/10.1126/science.289.5481.953, PMID: 10937999

775 Borst JG, Sakmann B. 1996. Calcium influx and transmitter release in a fast CNS
776 synapse. *Nature* **383**:431-434. DOI: https://doi.org/10.1038/383431a0, PMID: 8837774

777 Brockmann MM, Maglione M, Willmes CG, Stumpf A, Bouazza BA, Velasquez LM, Grauel
778 MK, Beed P, Lehmann M, Gimber N, Schmoranzer J, Sigrist SJ, Rosenmund C, Schmitz
779 D. 2019. RIM-BP2 primes synaptic vesicles *via* recruitment of Munc13-1 at hippocampal
780 mossy fiber synapses. *eLife* **8**:e43243. DOI: https://doi.org/10.7554/eLife.43243, PMID:
781 31535974

782 Brockmann MM, Zarebidaki F, Camacho M, Grauel MK, Trimbuch T, Südhof TC,
783 Rosenmund C. 2020. A Trio of Active Zone Proteins Comprised of RIM-BPs, RIMs, and
784 Munc13s Governs Neurotransmitter Release. *Cell Reports* **32**:107960-107960. DOI:
785 https://doi.org/10.1016/j.celrep.2020.107960, PMID: 32755572

786 Butola T, Alvanos T, Hintze A, Koppensteiner P, Kleindienst D, Shigemoto R, Wichmann
787 C, Moser T. 2021. RIM-Binding Protein 2 Organizes Ca^{2+} Channel Topography and
788 Regulates Release Probability and Vesicle Replenishment at a Fast Central Synapse.
789 *Journal of Neuroscience* **41**:7742-7767. DOI: https://doi.org/10.1523/JNEUROSCI.0586-
790 21.2021, PMID: 34353898

791 Castillo PE, Weisskopf MG, Nicoll RA. 1994. The role of Ca^{2+} channels in hippocampal
792 mossy fiber synaptic transmission and long-term potentiation. *Neuron* **12**:261-269. DOI:
793 https://doi.org/10.1016/0896-6273(94)90269-0, PMID: 8110457

794 Dodge FA, Rahamimoff R. 1967. Co-operative action a calcium ions in transmitter release
795 at the neuromuscular junction. *The Journal of physiology* **193**:419-432. DOI:
796 https://doi.org/10.1113/jphysiol.1967.sp008367, PMID: 6065887

797 Geiger JR, Jonas P. 2000. Dynamic control of presynaptic Ca^{2+} inflow by fast-inactivating
798 K^{+} channels in hippocampal mossy fiber boutons. *Neuron* **28**: 927-939. DOI:
799 https://doi.org/10.1016/s0896-6273(00)00164-1, PMID: 11163277

800 Grauel MK, Maglione M, Reddy-Alla S, Willmes CG, Brockmann MM, Trimbuch T,
801 Rosenmund T, Pangalos M, Vardar G, Stumpf A, Walter AM, Rost BR, Eickholt BJ,
802 Haucke V, Schmitz D, Sigrist SJ, Rosenmund C. 2016. RIM-binding protein 2 regulates
803 release probability by fine-tuning calcium channel localization at murine hippocampal
804 synapses. *PNAS* **113**:11615-11620. DOI: https://doi.org/10.1073/pnas.1605256113,
805 PMID: 27671655

806 Hallermann S, Pawlu C, Jonas P, Heckmann M. 2003. A large pool of releasable vesicles
807 in a cortical glutamatergic synapse. *PNAS* **100**:8975-8980. DOI:
808 https://doi.org/10.1073/pnas.1432836100, PMID: 12815098

809 Hibino H, Pironkova R, Onwumere O, Vologodskaia M, Hudspeth AJ, Lesage F. 2002.
810 RIM binding proteins (RBPs) couple Rab3-interacting molecules (RIMs) to voltage-gated
811 Ca^{2+} channels. *Neuron* **34**:411-423. DOI: https://doi.org/10.1016/s0896-6273(02)00667-0,
812 PMID: 11988172

813 Kaeser PS, Deng L, Wang Y, Dulubova I, Liu X, Rizo J, Südhof TC. 2011. RIM proteins
814 tether Ca^{2+} channels to presynaptic active zones via a direct PDZ-domain interaction. *Cell*
815 **144**:282-295. DOI: https://doi.org/10.1016/j.cell.2010.12.029, PMID: 21241895

816 Katz B. 1969. The release of neural transmitter substances. Liverpool University Press.
817 ISBN: 0853230609

818 Krinner S, Butola T, Jung S, Wichmann C, Moser T. 2017. RIM-Binding Protein 2
819 Promotes a Large Number of $Ca_V1.3$ Ca^{2+}-Channels and Contributes to Fast Synaptic
820 Vesicle Replenishment at Hair Cell Active Zones. *Frontiers in Cellular Neuroscience*
821 **11**:334. DOI: https://doi.org/10.3389/fncel.2017.00334, PMID: 29163046

822 Krinner S, Predoehl F, Burfeind D, Vogl C, Moser T. 2021. RIM-Binding Proteins Are
823 Required for Normal Sound-Encoding at Afferent Inner Hair Cell Synapses. *Frontiers in*
824 *molecular neuroscience* **14**:651935. DOI: https://doi.org/10.3389/fnmol.2021.651935,
825 PMID: 33867935

826 Li L, Bischofberger J, Jonas P. 2007. Differential gating and recruitment of P/Q-, N-, and
827 R-type Ca^{2+} channels in hippocampal mossy fiber boutons. *Journal of Neuroscience*
828 **27**:13420-13429. DOI: https://doi.org/10.1523/JNEUROSCI.1709-07.2007, PMID:
829 18057200

830 Lindau M, Neher E. 1988. Patch-clamp techniques for time-resolved capacitance
831 measurements in single cells. *Pflügers Archiv* **411**:137-146. DOI:
832 https://doi.org/10.1007/BF00582306, PMID: 3357753

833 Liu KS, Siebert M, Mertel S, Knoche E, Wegener S, Wichmann C, Matkovic T,
834 Muhammad K, Depner H, Mettke C, Bückers J, Hell SW, Müller M, Davis GW, Schmitz D,
835 Sigrist SJ. 2011. RIM-binding protein, a central part of the active zone, is essential for
836 neurotransmitter release. *Science* **334**:1565-1569. DOI:
837 https://doi.org/10.1126/science.1212991, PMID: 22174254

838 Luo F, Liu X, Südhof TC, Acuna C. 2017. Efficient stimulus-secretion coupling at ribbon
839 synapses requires RIM-binding protein tethering of L-type Ca^{2+} channels. *Proceedings of*
840 *the National Academy of Sciences* **114**:E8081-E8090. DOI:
841 https://doi.org/10.1073/pnas.1702991114, PMID: 28874522

842 Midorikawa M, Sakaba T. 2017. Kinetics of Releasable Synaptic Vesicles and Their
843 Plastic Changes at Hippocampal Mossy Fiber Synapses. *Neuron* **96**:1033-1040.e3. DOI:
844 https://doi.org/10.1016/j.neuron.2017.10.016, PMID: 29103807

845 Miki T, Malagon G, Pulido C, Llano I, Neher E, Marty A. 2016. Actin- and Myosin-
846 Dependent Vesicle Loading of Presynaptic Docking Sites Prior to Exocytosis. *Neuron*
847 **91**:808-823. DOI: https://doi.org/10.1016/j.neuron.2016.07.033, PMID: 27537485

848 Mittelstaedt T, Schoch S. 2007. Structure and evolution of RIM-BP genes: identification of
849 a novel family member. *Gene* **403**:70-79. DOI:
850 https://doi.org/10.1016/j.gene.2007.08.004, PMID: 17855024

851 Müller M, Genç Ö, Davis GW. 2015. RIM-binding protein links synaptic homeostasis to
852 the stabilization and replenishment of high release probability vesicles. *Neuron* **85**:1056-
853 1069. DOI: https://doi.org/10.1016/j.neuron.2015.01.024, PMID: 25704950

854 Neher E, Brose N. 2018. Dynamically Primed Synaptic Vesicle States: Key to Understand
855 Synaptic Short-Term Plasticity. *Neuron* **100**:1283-1291. DOI:
856 https://doi.org/10.1016/j.neuron.2018.11.024, PMID: 30571941

857 Pelkey KA, Topolnik L, Lacaille J-C, McBain CJ. 2006. Compartmentalized Ca^{2+} channel
858 regulation at divergent mossy-fiber release sites underlies target cell-dependent plasticity.
859 *Neuron* **52**:497-510. DOI: https://doi.org/10.1016/j.neuron.2006.08.032, PMID: 17088215

860 Petzoldt AG, Götz TWB, Driller JH, Lützkendorf J, Reddy-Alla S, Matkovic-Rachid T, Liu
861 S, Knoche E, Mertel S, Ugorets V, Lehmann M, Ramesh N, Beuschel CB, Kuropka B,
862 Freund C, Stelzl U, Loll B, Liu F, Wahl MC, Sigrist SJ. 2020. RIM-binding protein couples
863 synaptic vesicle recruitment to release sites. *Journal of Cell Biology* **219**:e201902059.
864 DOI: https://doi.org/10.1083/jcb.201902059, PMID: 32369542

865 Rollenhagen A, Sätzler K, Rodríguez EP, Jonas P, Frotscher M, Lübke JHR. 2007.
866 Structural determinants of transmission at large hippocampal mossy fiber synapses.
867 *Journal of Neuroscience* **27**:10434-10444. DOI:
868 https://doi.org/10.1523/JNEUROSCI.1946-07.2007, PMID: 17898215

869 Sakamoto H, Ariyoshi T, Kimpara N, Sugao K, Taiko I, Takikawa K, Asanuma D, Namiki
870 S, Hirose K. 2018. Synaptic weight set by Munc13-1 supramolecular assemblies. *Nature*
871 *neuroscience* **21**:41–49. DOI: https://doi.org/10.1038/s41593-017-0041-9, PMID:
872 29230050

873 Sakamoto H, Kimpara N, Namiki S, Hamada S, Ohtsuka T, Hirose K. 2022. Synapse type-
874 specific molecular nanoconfigurations of the presynaptic active zone in the hippocampus

875 identified by systematic nanoscopy [unpublished manuscript]. *bioRxiv* 2022.03.11.483942.
876 DOI: https://doi.org/10.1101/2022.03.11.483942

877 Schneggenburger R, Meyer AC, Neher E. 1999. Released fraction and total size of a pool
878 of immediately available transmitter quanta at a calyx synapse. *Neuron* **23**:399-409. DOI:
879 https://doi.org/10.1016/s0896-6273(00)80789-8, PMID: 10399944

880 Schneggenburger R, Neher E. 2000. Intracellular calcium dependence of transmitter
881 release rates at a fast central synapse. *Nature* **406**: 889-893. DOI:
882 https://doi.org/10.1038/35022702, PMID: 10972290

883 Südhof TC. 2012. The presynaptic active zone. *Neuron* **75**:11-25. DOI:
884 https://doi.org/10.1016/j.neuron.2012.06.012, PMID: 22794257

885 Tang AH, Chen H, Li TP, Metzbower SR, MacGillavry HD, Blanpied TA. 2016. A trans-
886 synaptic nanocolumn aligns neurotransmitter release to receptors. *Nature* **536**:210-214.
887 DOI: https://doi.org/10.1038/nature19058, PMID: 27462810

888 Thanawala MS, Regehr WG. 2013. Presynaptic calcium influx controls neurotransmitter
889 release in part by regulating the effective size of the readily releasable pool. *Journal of*
890 *Neuroscience* **33**:4625-4633. DOI: https://doi.org/10.1523/JNEUROSCI.4031-12.2013,
891 PMID: 23486937

892 von Gersdorff H, Matthews G. 1996. Calcium-dependent inactivation of calcium current in
893 synaptic terminals of retinal bipolar neurons. *Journal of Neuroscience* **16**:115-122. DOI:
894 https://doi.org/10.1523/JNEUROSCI.16-01-00115.1996, PMID: 8613777

895 Vyleta NP, Jonas P. 2014. Loose coupling between Ca^{2+} channels and release sensors at
896 a plastic hippocampal synapse. *Science* **343**:665-670. DOI:
897 https://doi.org/10.1126/science.1244811, PMID: 24503854

898 Wadel K, Neher E, Sakaba T. 2007. The coupling between synaptic vesicles and Ca^{2+}
899 channels determines fast neurotransmitter release. *Neuron* **53**:563-575. DOI:
900 https://doi.org/10.1016/j.neuron.2007.01.021, PMID: 17296557

901 Wang Y, Sugita S, Südhof TC. 2000. The RIM/NIM family of neuronal C2 domain
902 proteins. Interactions with Rab3 and a new class of Src homology 3 domain proteins.

903 *Journal of Biological Chemistry* **275**:20033-20044. DOI:
904 https://doi.org/10.1074/jbc.M909008199, PMID: 10748113

905 Wenzel HJ, Cole TB, Born DE, Schwartzkroin PA, Palmiter RD. 1997. Ultrastructural
906 localization of zinc transporter-3 (ZnT-3) to synaptic vesicle membranes within mossy fiber
907 boutons in the hippocampus of mouse and monkey. *PNAS* **94**:12676-12681. DOI:
908 https://doi.org/10.1073/pnas.94.23.12676, PMID: 9356509
909